

Structural Disorder in Two-Dimensional Network-Forming Materials



David Ormrod Morley
Balliol College
University of Oxford

A thesis submitted for the degree of
Doctor of Philosophy

Trinity 2020

Contents

1 Targeted Optimisation of Atomic Networks	1
1.1 Disorder in Two-Dimensional Networks	1
1.2 Targeted Optimisation Algorithm	2
1.2.1 Dual Space Implementation	4
1.3 Mapping Configurational Space	5
1.3.1 Limits of the Aboav-Weaire Parameter	6
1.3.2 Structure and Energetics	7
1.4 Ring Percolation in Amorphous Graphene	10
1.4.1 Percolation Theory and Clustering	11
1.4.2 Percolation in Disordered Networks	13
1.4.3 Percolation Phase Diagram of Amorphous Graphene	14
1.5 Chapter Conclusions	18
Appendices	
References	21

List of Notes By David

1	fig here maybe, and for 8-4-8	9
---	---	---

List of Notes By Mark

1 | Modelling Bilayer Materials

A computationally tractable Monte Carlo method using triangle rafts is developed to generate bilayers of SiO_2 and related materials. The method allows defect free networks of any given shape to be grown with both tuneable ring statistics and topologies, controlled by a combination of the “allowed” rings and the effective growth “temperature”. Configurations are generated with Aboav-Weaire parameters commensurate with those obtained from an analysis of experimental configurations, improving significantly on previous methods. The ability to efficiently grow configurations allows exploration of the structural basis of Lemaître’s law, where the commonly observed value of $p_6 \approx 0.4$ is presented as a balance between entropic and enthalpic factors. The deviations of ring areas from the ideal values are discussed and the relative insensitivity of the ring area to relatively strong distortions is highlighted.

1.1 Bilayer Materials

An important class of two-dimensional materials which have emerged in the 21st century are bilayers of silica, SiO_2 , and related species [11]. These can be prepared experimentally by chemical vapour deposition on metal and graphene supports [4, 5]. As in the three-dimensional glass, the basic building blocks of silica bilayers are vertex sharing SiO_4 tetrahedra, maintaining full coordination for all atoms in the bulk [22]. These are arranged such that three of the vertices are connected to tetrahedra in the same layer, with the final vertex being shared between layers acting as a “bridge” (figure ??). A consequence of these bridging oxygen atoms is to enforce a symmetry plane between the upper and lower layers.

Topologically, the symmetry plane means that these materials can be viewed as effective two-dimensional networks. Taking one of the layers, without the bridging

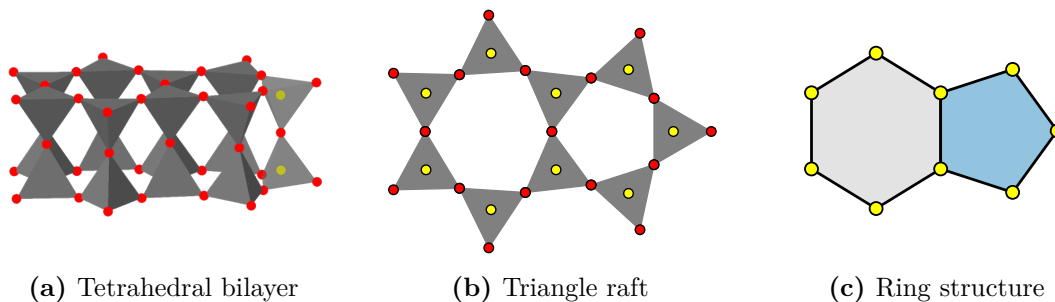


Figure 1.1: Silica bilayers of vertex sharing tetrahedra in (a) can be represented as a two-dimensional triangle raft in (b). Silicon and oxygen atoms are coloured yellow and red respectively. The ring structure then emerges from the three-coordinate network comprising the silicon atoms, (c).

oxygens, and projecting the atoms onto the horizontal plane reveals a representation of vertex sharing triangles, referred to as a triangle raft (figure ??). The ring structure then emerges from the three-coordinate network formed by connecting the silicon atoms of adjacent triangles as in figure ??.

Indeed, scanning tunnelling microscopy (STM) has been used to directly visualise the ring structure in silica bilayers, revealing both crystalline and glassy arrangements and even the interface between the two [128, 129].

More recently experimentalists have also succeeded in synthesising bilayers of germania, GeO_2 [7, 8]. [Add a bit more experimental context here, discuss with Mark](#)

1.2 Review of Existing Methods

As mentioned in the introduction, both *ab initio* methods and classical molecular dynamics have been used in computational studies of silica bilayers, which often require a starting atomistic configuration [20–22, 28]. One approach is to simply take an experimental sample as the starting structure. Whilst this may be on the surface the best solution, the experimental configurations may contain defects or areas where the image is corrupted *i.e.* the configuration may not be “pristine”. Additionally, the location of each atom has an associated uncertainty which leads to discrepancies in the observed bond lengths and angles, which can be compounded by any out-of-plane distortions. Whilst computational refinement can attenuate these problems [23, 130], there remains the more fundamental question of how

“typical” the available images are from experiment, as STM provides exceptional information but only on relatively small sample sizes. Computational techniques can therefore prove a valuable tool for generating a large number of high-quality configurations and corroborating experimental information.

One current approach is to transform amorphous graphene configurations [22]. Here amorphous samples of carbon are generated using a bond switching method (as outlined in section ??), before the carbon atoms are swapped from silicon and decorated with oxygens. Whilst this is a valid approach, the method assumes that the two materials are topologically equivalent. This is likely an oversimplification, as the presence of the bridging oxygens in silica afford the structure increased flexibility when compared to the carbon analogue. This likely explains why this method has struggled to mirror experimentally observed values of the ring statistics and Aboav-Weaire parameter, with small and large ring proportions being under-estimated [29].

An alternative approach is to use molecular dynamics coupled with an effective pair potential to obtain viable configurations [28]. Such methods are relatively common, having been employed previously to study amorphous graphene [104]. Such methods offer the potential for generating realistic configurations but are difficult to control as the cooling rates which must be applied are necessarily huge compared to experimental rates. A potential artefact of the high cooling rates is the effectively freezing in of defect states, either in terms of local coordination environments or highly-strained (three-membered) rings. In addition, as with the method above, such methods appears to systematically underestimate the Aboav-Weaire parameter, indicative of too little structural ordering.

1.3 Triangle Raft Method

The motivation of this work was to develop a construction algorithm to generate samples of silica bilayers which can capture the full two-dimensional network topology; both the ring distribution *and* correlations. The model should be able to explore all phases from crystalline to amorphous yet computationally efficient enough to produce configurations suitable for further high throughput calculations.

To achieve this a grow-from-seed Monte Carlo algorithm has been developed, where rings are individually added to build a triangle raft. This approach takes inspiration from the first hand-built models, which have been noted to bear close resemblance to experimental structures [131, 132]. Such models were superseded by computational techniques designed to generate periodic configurations. However, the recent development in techniques to simulate aperiodic samples, such as sliding boundary conditions for molecular dynamics [133], makes this constraint no longer essential, and benefit may be gained from the added freedom of an aperiodic model.

1.3.1 Potential Model

As explained in figure ?? it is possible to capture the full topology of silica bilayers with a simplified representation consisting of a network of vertex-sharing SiO_3 triangles. As the focus of this chapter is on generating a large number of samples with varying ring statistics, working with this reduced representation is sufficient, as it provides a computationally efficient way to produce networks with the required *topology*. The precise *geometry* of the bilayer can be refined with advanced optimisation techniques if required [134].

In order to simulate bilayer systems in two dimensions, a suitable potential model is needed which captures the essential physics of the system: the local triangular environment of the SiO_3 units and the relative energies of rings of different sizes. The model used here is modified from a relatively simple potential used in all-atom bilayer calculations [22, 23], a schematic for which is given in figure ?. Each SiO_3 unit has a harmonic potential acting between all three Si–O pairs, and the three nearest-neighbour O–O pairs, given by:

$$\mathcal{U}_{ij} = \frac{K}{2} (r_{ij} - r_{ij}^0)^2, \quad (1.1)$$

where K is a constant, r_{ij} is the interatomic separation and r_{ij}^0 the equilibrium interatomic separation between i, j . The spring constant, K , is set to be very stiff, whilst the equilibrium separations are set according to elemental species such that $r_{\text{OO}}^0 = \sqrt{3} r_{\text{SiO}}^0$, maintaining a set of ideal SiO_3 triangles.

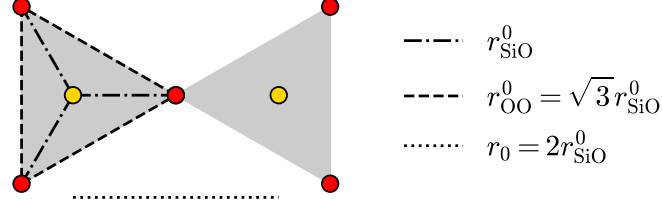


Figure 1.2: Schematic of the potential model in triangle rafts. Stiff harmonic springs (dashed and dashed-dotted lines) preserve the triangular subunits, whilst the shifted and cut 24-12 potential (dotted line) maintains an equilibrium angle of 120° between neighbouring subunits.

The Si–O–Si angle, which determines the strain associated with different ring sizes, is controlled by a shifted and cut 24-12 potential of the form:

$$\mathcal{U}_{ij} = \begin{cases} \epsilon \left[\left(\frac{r_0}{r_{ij}} \right)^{24} - 2 \left(\frac{r_0}{r_{ij}} \right)^{12} \right] + \epsilon & r_{ij} \leq r_0 \\ 0 & \text{otherwise} \end{cases} \quad (1.2)$$

where ϵ is a constant and r_{ij} is now the Si–Si separation between atoms in adjacent triangles. It is the value of r_0 which sets the Si–O–Si angle at which strain begins to be felt and therefore the relative ring energies. Taking the hexagonal lattice as being the zero in energy it follows that $r_0 = 2r_{\text{SiO}}$. Rings which deviates increasingly from the ideal hexagon will therefore incur an increasingly energetic penalty.

To summarise, the primary aim here is to generate topologies suitable for later investigation using more detailed (and hence more accurate but more computationally-demanding) potential models. As a result, the harmonic springs simply control the local (triangular) geometries whilst the 24-12 potential controls the repulsion between these local polyhedra. These functions are chosen as deliberately simple to improve computational efficiency and achieve high throughput of idealised networks. Furthermore, the parameters K and ϵ need have no direct physical meaning, simply controlling the meaning of the system “temperature” as discussed below. The only requirement is that they generate energies of the same magnitude to allow for efficient structural evolution.

1.3.2 Algorithmic Details

Using the model detailed above, a Monte Carlo construction algorithm has been developed which allows two-dimensional networks to be built ring by ring in the

shape of a specified function. The main steps of the algorithm are outlined below:

1. Take a starting seed, such as a single ring or experimental configuration
2. Select triangles on which to build the next ring (see figure ??)
 - (a) Overlay a function on the network (*e.g.* circle, square)
 - (b) Check for atoms with dangling bonds lying inside the function region
 - (c) If no such atoms exist, systematically increase the function size until an atom is found
 - (d) Find the next nearest atoms which also have a dangling bonds
 - (e) Choose the two triangles that correspond to the largest starting ring size
3. Determine the probability of constructing rings of different sizes
 - (a) Build trial rings in the range k_{\min} to k_{\max} (see figure ??)
 - (b) Geometry optimise the local structure and calculate minimised potential energy (as explained in section ??)
 - (c) Calculate the probabilities of each ring occurring, P_k , equation (??)
4. Accept single trial ring according to the probability distribution
5. Repeat steps ?? \rightarrow ?? until the target number of rings is reached

The probability of a ring of size k being accepted, P_k , is given by the equation:

$$P_k = \frac{\exp [-(\mathcal{U}_k - \mathcal{U}_0) / T]}{\sum_k \exp [-(\mathcal{U}_k - \mathcal{U}_0) / T]}, \quad (1.3)$$

where \mathcal{U}_k and \mathcal{U}_0 correspond to the energy of the trial structure and lowest energy of all trial structures respectively, and T is a “temperature”. The parameter T controls how easily the potential energy landscape can be explored, and therefore how accessible strained rings become. In the low T limit, the acceptance probabilities are dominated by the energy term, and the rings which are selected will be those with the lowest energy. Note that this is not necessarily the 6-ring, but rather is



Figure 1.3: Panel (a) shows how triangles used to construct a ring are initially selected. There are no atoms with dangling bonds within the first search region (blue dashed line), and so the search area is extended (red dashed line), where triangles A and B are found. Panel (b) gives the three possibilities for the triangles that will form part of the constructed ring: A–C–D–B, A–E, B–F. As A–C–D–B corresponds to the largest starting ring size this is selected.

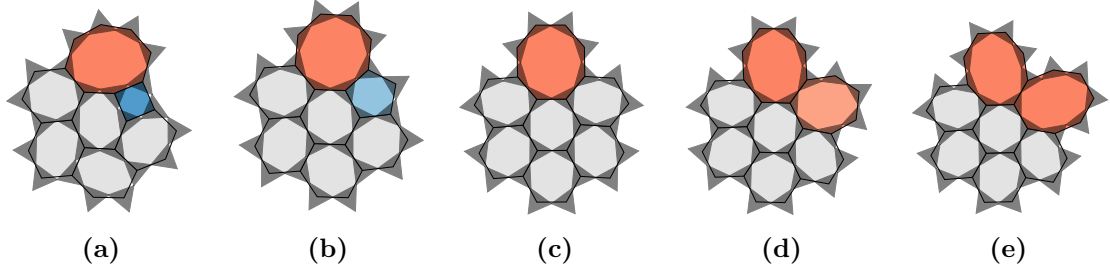


Figure 1.4: Geometry optimised structures for trial rings in the range $k = 4 - 8$. The ring structure is shown along with the SiO_3 triangle

Table 1.1: Variation of acceptance probabilities with temperature for the configurations in figure ??.

P_k	4	5	6	7	8
$T = 10^{-4}$	0.0000	1.0000	0.0000	0.0000	0.0000
$T = 10^{-3}$	0.0000	0.8837	0.1162	0.0001	0.0000
$T = 10^{-2}$	0.0336	0.4104	0.3351	0.1659	0.0550
$T = 10^{-1}$	0.1734	0.2227	0.2183	0.2034	0.1822
$T = 10^0$	0.1973	0.2023	0.2018	0.2004	0.1982

dependent on the local environment. On the other hand, in the high T limit, the acceptance probabilities are approximately equal, and rings are selected on a more random basis. This is demonstrated in table ??, using the example configurations from figure ?. The “temperature” parameter is therefore the primary method for controlling the distribution of ring sizes in constructed networks.

1.4 Properties of Triangle Rafts

The triangle raft method is evaluated in terms of its effectiveness in producing configurations which accurately replicate the network properties of experimental silica bilayers *i.e.* the ring statistics and Aboav-Weaire parameter. It is also compared against the existing methods introduced in section ??, namely generation from amorphous graphene or molecular dynamics. This is performed in the wider context of systematically varying the model parameters to explore the behaviour of generic networks of this type.

1.4.1 Network Growth

The triangle raft method is robust and controllable, and is able to generate configurations with tuneable ring statistics and topologies. Results will largely focus on the system where $k = 4 - 10$, denoted $\{4, 10\}$, mimicking the experimentally observed range for silica bilayers. Six example configurations are given in figure ??, which are generated with a range of temperatures and growth geometries. Figures ??-?? provide a good qualitative analysis of the effect of temperature on the ring structure. At low temperature a phase boundary can be seen separating crystalline and amorphous regions, as seen in experimental silica bilayers [129]. In these samples although the proportion of small and large rings is low, their positions are highly correlated and chain structures of alternating rings sizes are clearly present. These motifs are reminiscent of defects found in a wide range of materials, including amorphous graphene and thin silicon and germanium oxides [3, 7, 11, 20]. The increase in temperature is coupled with the emergence of rings of more extreme sizes and regions which could be viewed as nano-crystalline are dispersed. The high temperature limit reveals a fully amorphous structure.

Figures ?? and ?? give examples of the diverse geometries in which samples may be constructed. It is interesting to note that even “difficult” shapes, such as those containing concave regions and cusps, do not prevent growth. Although the shape does not affect the network topology and is in a sense arbitrary, certain calculations may benefit from the different configurational shapes. For instance,

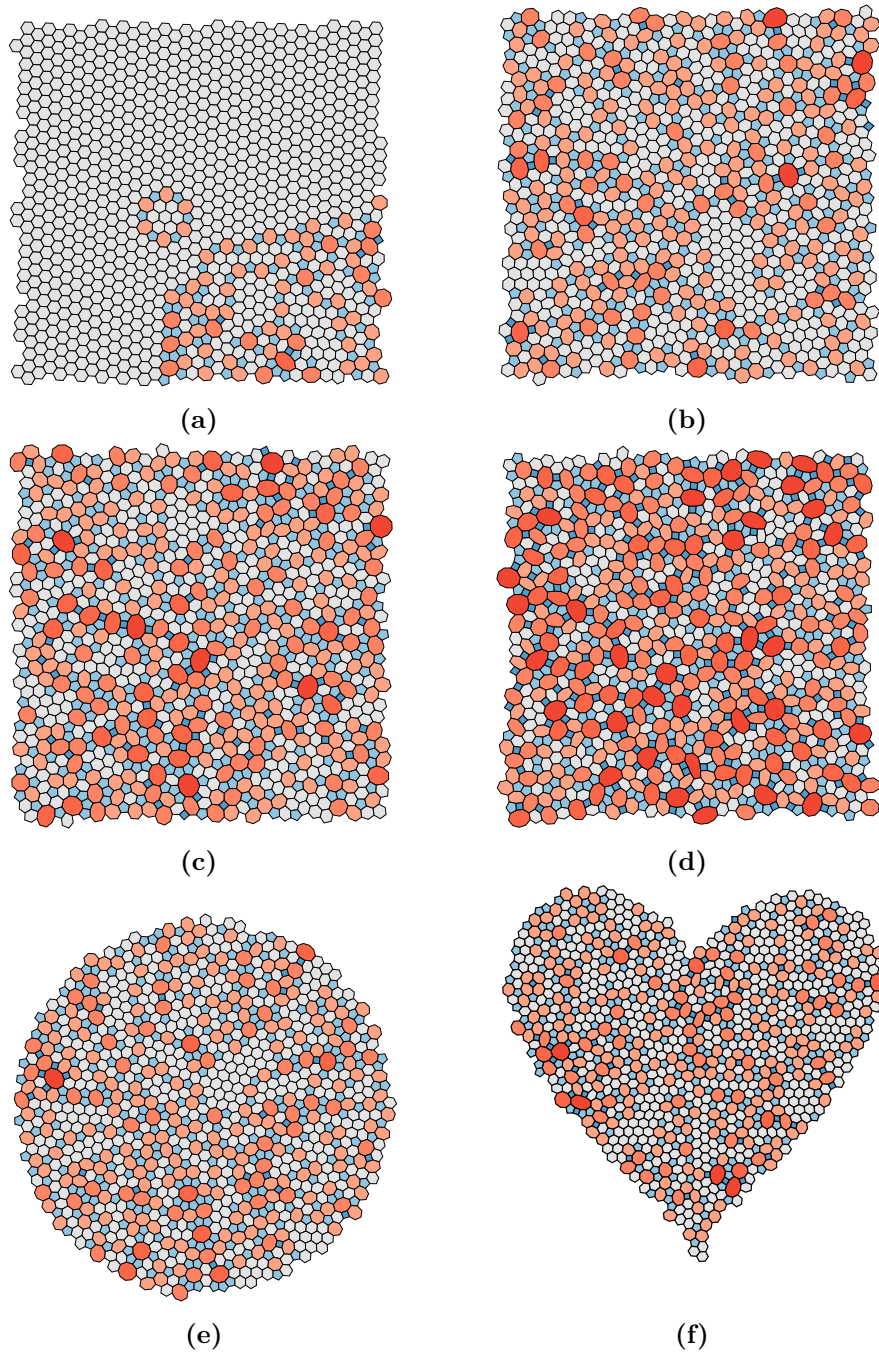


Figure 1.5: Example 1,000 ring configurations generated with different temperatures and shapes. Panels (a) through (d) show square lattices grown at $T = 10^{-4.0}$, $10^{-3.0}$, $10^{-2.5}$, $10^{-2.0}$ respectively. The samples show the increasing diversity in ring structure as temperature is increased. Panels (e), (f) show configurations with alternative lattice shapes at $T = 10^{-3.0}$, demonstrating the flexibility of the method in growing samples with variable geometries. Rings are coloured according to size with $k < 6$ as blue, $k = 6$ as grey and $k > 6$ as red.

molecular dynamics with sliding boundary conditions requires fitting of a smooth function to the sample perimeter, which is facilitated by having a near-circular form. Other areas such as percolation problems may benefit from square samples.

1.4.2 Network Properties

The quantitative relationship between temperature and ring structure was investigated for three systems of varying ring size ranges; $\{5, 7\}$, $\{4, 8\}$ and $\{4, 10\}$. For each system, 100 samples consisting of 1000 rings were grown at temperatures between $T = 10^{-4.5} \rightarrow 10^{-1.5}$. The evolution of the combined ring statistics with temperature is presented in figure ?? . Figures ??-?? give bar representations of the ring size distributions for the three systems, which show different behaviours. For $\{5, 7\}$ the individual p_k are all monotonically increasing ($k \neq 6$) or decreasing ($k = 6$) functions, but both $\{4, 8\}$ and $\{4, 10\}$ have p_k containing maxima. Additionally, both $\{5, 7\}$ and $\{4, 8\}$ achieve uniform distributions in the high temperature limit but $\{4, 10\}$ does not.

This disparity in behaviour can largely be traced back to the constraint of Euler's theorem. As $\{5, 7\}$ comprises of just three ring sizes, Euler's formula demands that $p_5 = p_7 = (1 - p_6) / 2$ and so the system is relatively well defined. Hence, as the 5 and 7-rings are more strained than the 6-ring, p_5 and p_7 show a systematic increase with temperature. Furthermore, the uniform equilibrium distribution can only satisfy Euler's formula when the ring size range is symmetric about 6, as is observed for $\{5, 7\}$ and $\{4, 8\}$. The form of the ring statistics at intermediate temperatures and for $\{4, 10\}$ follow the maximum entropy solutions according to Lemaître's law, discussed in section ?? and later in this section.

The ring distribution for $\{4, 10\}$ is also shown as a function of temperature in figure ??, along with the value of the Aboav-Weaire parameter, α , allowing for more facile comparison with experiment. The temperature which gives the best agreement between our model and amorphous experimental samples is highlighted by the vertical dashed line. The values of p_k and α are provided in table ??, alongside results from two experimental samples. It is evident that the model can

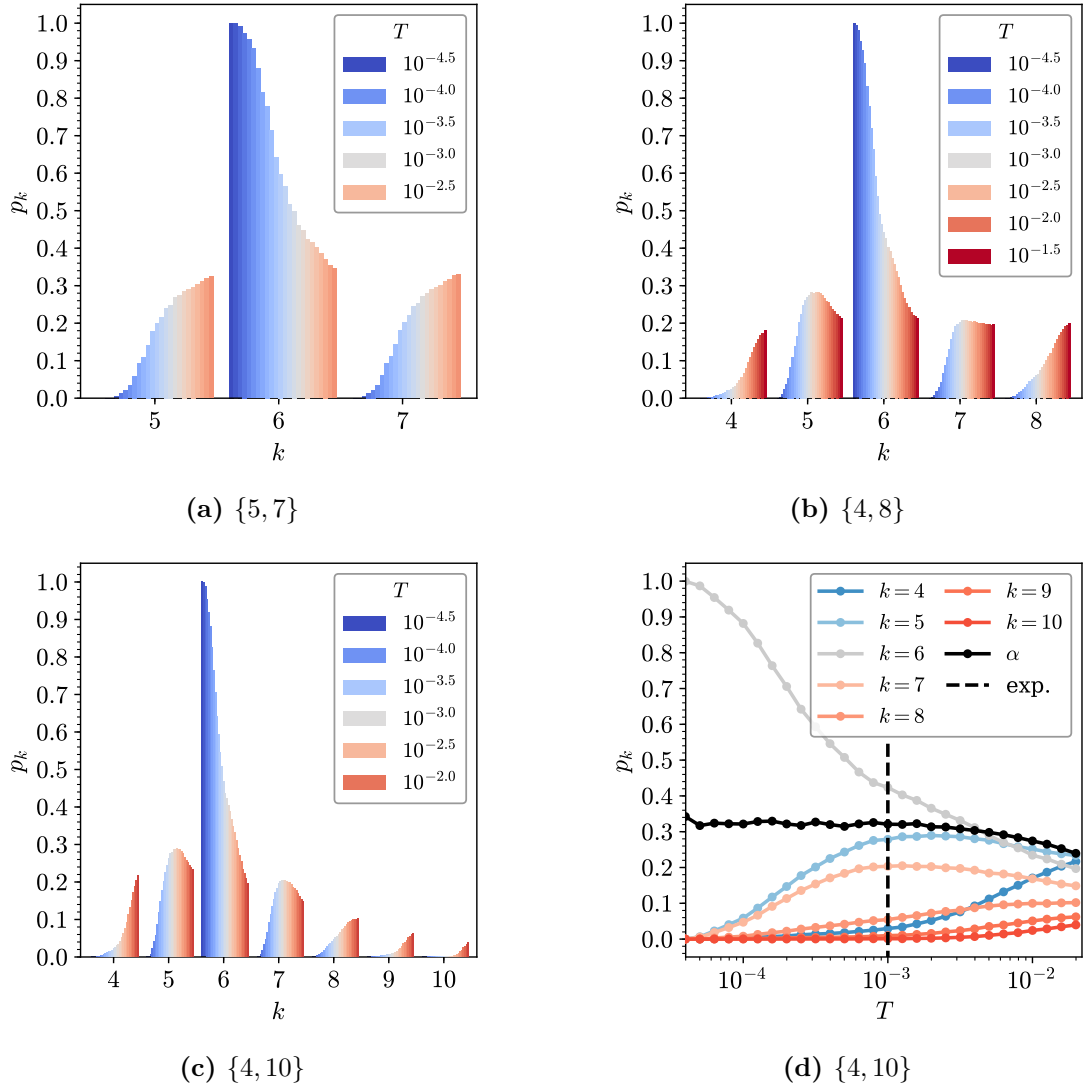


Figure 1.6: Variation in ring statistics with temperature over a given allowable k -range. Panels (a)-(c) show bar graph representations of the ring statistics, coloured by temperature, for the $\{5, 7\}$, $\{4, 8\}$ and $\{4, 10\}$ systems, respectively. Panel (d) gives an alternative line graph representation of the ring statistics for $\{4, 10\}$, coloured by ring size, along with the Aboav-Weaire parameter. The temperature which gives the best match to the experimentally observed amorphous region is also highlighted (vertical black dashed line).

be successfully tuned to match the topology of the experimental system. Not only are the ring distributions in very good accordance, but also the ring correlations, which have until now proved difficult to capture. This provides confidence that this simplified but physically motivated triangle raft model is able to reproduce the behaviour of real systems.

Table 1.2: Comparison of silica bilayer samples from experiment, computational modelling and theory.

	Experiment		Computation				Theory
	Ru(0001) [132]	Graphene [4]	MC ^a [29]	MC ^a [29]	MD ^b [28]	TR ^c	Lemaître [62]
N	317	444	216	418	16×85000	1000×100	–
p_3	0.0000	0.0000	0.00	0.00	0.0038	0.0000	0.0000
p_4	0.0379	0.0383	0.02	0.00	0.0537	0.0295	0.0280
p_5	0.2744	0.2725	0.33	0.37	0.2686	0.2786	0.2834
p_6	0.4448	0.4189	0.37	0.32	0.3773	0.4234	0.4200
p_7	0.1609	0.2117	0.21	0.25	0.2224	0.2034	0.2077
p_8	0.0757	0.0495	0.07	0.06	0.0602	0.0544	0.0518
p_9	0.0063	0.0068	<0.01	0.00	0.0118	0.0097	0.0082
p_{10}	0.0000	0.0023	0.00	0.00	0.0018	0.0010	0.0009
$p_{>10}$	0.0000	0.0000	0.00	0.00	0.0004	0.0000	0.0000
μ_2	0.9460	0.9333	0.94	0.86	1.1302	0.9208	0.8985
α	0.32	0.33	0.18	0.23	0.25	0.32	–

Note: Each method is given alongside the number of rings in the sample, N , followed by the ring statistics, p_k , the second moment of the ring statistics, μ_2 , and the Aboav-Weaire parameter, α

^a Bond switching Monte Carlo (graphene potential) ^b Molecular dynamics ^c Triangle rafts, this work, $T = 10^{-3}$

Table ?? also lists the ring statistics obtained from previous computational studies which used both Monte Carlo and molecular dynamics methods. As mentioned in the review of these methods above, neither fully succeeds in accurately capturing the topology of silica bilayers. Kumar *et al.* attempted to transform an amorphous graphene structure generated from bond switching Monte Carlo into a silica bilayer. The ring statistics of the resulting structure were approximately correct, but the proportion of 5- and 6- rings over- and under-estimated respectively. In addition the Aboav-Weaire parameter was substantially lower than experiment, indicating a relative lack of structure in the ring ordering. The origin of these discrepancies is likely the use of a graphene potential model. The increased stiffness of the carbon network (which unlike silica lacks bridging oxygens) means a high temperature must be used to obtain an amorphous structure with the required disorder. This leads to heavily distorted rings (as noted in the original paper) which reduces the requirement for small rings to be adjacent to large.

Roy *et al.* have an alternative approach of generating configurations with an effective pair potential and molecular dynamics. As can be seen the ring statistics are closer to the experimental values, but now contain artefacts, with a significant fraction of highly strained 3-membered rings and large rings up to $k = 14$. These manifest as a result of the artificially high cooling rates in the computational studies which trap defect states in the configurations. Once again the final Aboav-Weaire parameter, α , is underestimated.

It is worth re-emphasising here that the triangle raft method is able to replicate experimental values of both p_k and α , due to its tuneable approach and “organic” growth mechanism, where sample formation is not influenced by enforced periodicity. Beyond this, the controllable nature of the method also allows insight into key questions about silica bilayers, for instance the form of the ring distribution in this amorphous phase. As detailed in section ??, the maximum entropy ring distribution can be calculated numerically given the value of p_6 . For example, table ?? gives the maximum entropy solution for $p_6 = 0.42$, which agrees very well with the results

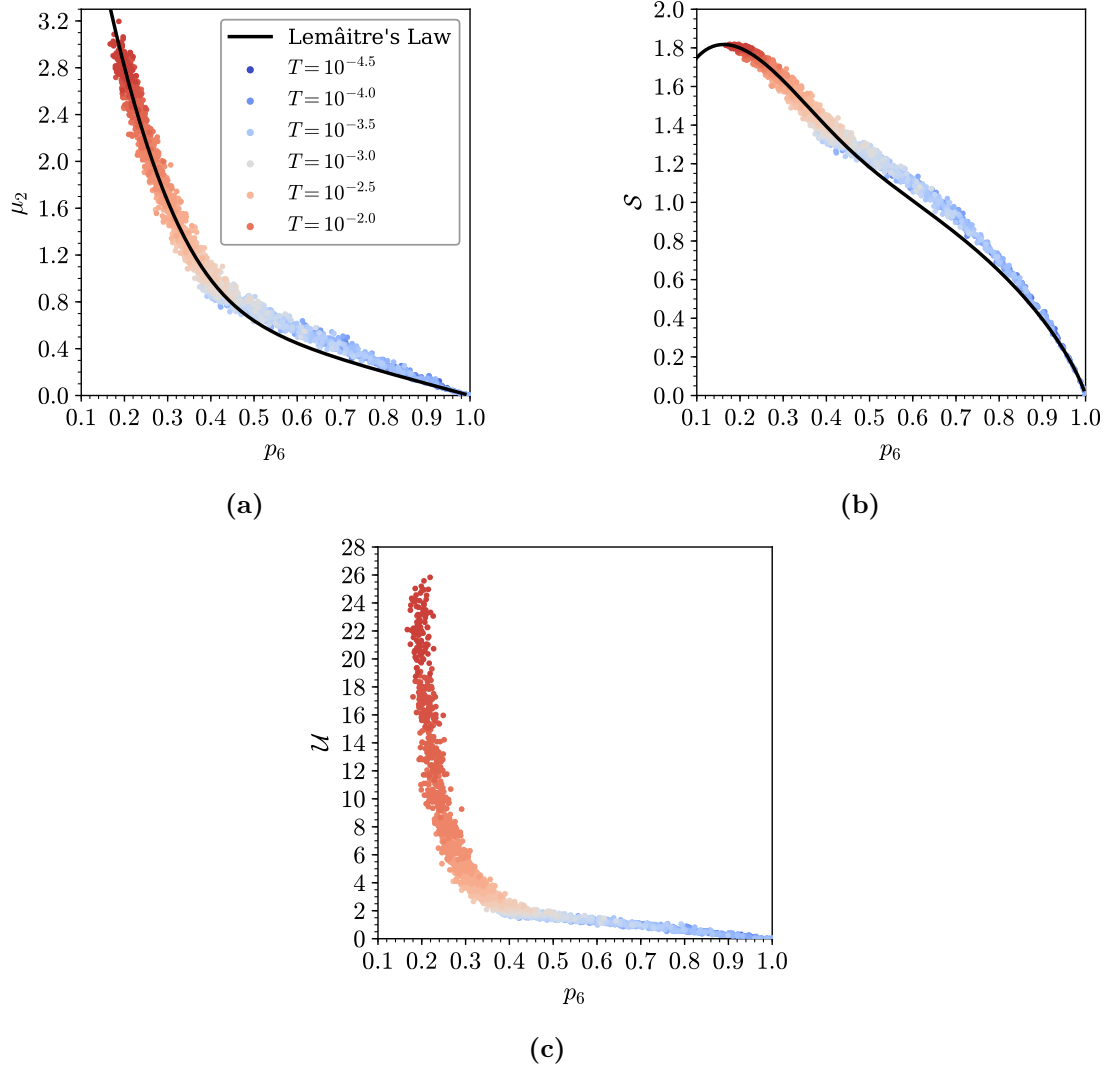


Figure 1.7: Evolution of ring statistics (a), entropy (b) and potential energy (c) of triangle rafts with temperature. The experimental value of $p_6 \approx 0.4$ occurs just before the exponential increase in potential energy, reflecting the balance of energetic and entropic factors.

from triangle rafts and experiment. This second moment of the distribution, μ_2 , is then uniquely related to p_6 via Lemaître's law, shown as the black line in in figure ??.

However, Lemaître's law gives no information on why a particular maximum entropy distribution is found for a given system. The triangle raft method allows systematic generation of configurations with different p_6 values by tuning the temperature parameter. The resulting configurations follow Lemaître's law across the entire temperature range. Figures ?? gives the results from the individual 1000 ring samples, coloured by temperature. Figures ?? and ?? compare the

observed μ_2 and \mathcal{S} (entropy) of the generated configurations to those expected from Lemaître’s law, showing the law provides a good fit, with only a small deviation observed for $p_k > 0.5$.

Figure ?? plots the geometry optimised potential energy of the samples against p_6 , which increases as the ring sizes become more diverse. The curve is split into two regimes, with gradual increase in energy from $p_6 = 1.0 \rightarrow 0.4$ followed by exponential increase for $p_6 < 0.4$. This is consistent with the information in figure ?? which shows that below $p_6 \approx 0.4$, not only does the number of extreme ring sizes increase rapidly, but they become less correlated with a lower α , decreasing the number of favourable small-large ring pairings.

It can now be proposed why the experimental amorphous distributions are found with a value of $p_6 \approx 0.4$. The system aims to maximise entropy by obtaining a ring distribution along the Lemaître curve with the minimum p_6 possible. However, for $p_6 < 0.4$ the energetic cost becomes prohibitively large, as higher entropy distributions can only be achieved by increasing the proportion of extreme ring sizes at the expense of relatively low strain 5- and 7- rings. Interestingly it is also evident why no configurations are present below $p_6 \approx 0.16$, even at the highest temperature. Below this point, the entropy of the $\{4, 10\}$ system decreases whilst the energy continues to rise and so there is no driving force to sample this area of phase space.

1.4.3 Physical Properties

As an additional check that the developed triangle raft model behaves physically, the angle distribution between adjacent SiO_3 units, $f(\theta)$, was calculated for the $\{4, 10\}$ system across the range of temperatures studied. The results are summarised in figure ?. The angle distributions are necessarily symmetric about 120° , as each triangle pair contributes two complementary angles. At lower temperatures the distribution is dominated by angles close to 120° , as a consequence of the large proportion of near strainless six membered rings. Furthermore, at the temperature corresponding to the amorphous experimental region, $T = 10^{-3}$, the distribution has a similar extent to the angle distribution found in experimental samples (see

for example figure 7 reference [28]). However, as the temperature increases, the form of $f(\theta)$ does not simply broaden as might be expected, but becomes bimodal. This can be rationalised by considering the angles that would be present in regular polygons of different sizes, marked by vertical lines in figure ???. These ideal angles are clustered away from the mean value of 120° , and hence increasing the diversity of ring sizes through temperature acts to shift the most commonly observed angles from the central value of 120° . It is therefore interesting to note that increasing structure in the angle distribution does not necessarily translate to increased order in the atomic configurations.

A final check comes from examining the ring areas in the generated configurations. Inspection of amorphous experimental samples reveals that the rings appear highly regular in shape. This can be quantified by determining the average dimensionless area for each ring size, A_k , and comparing it to the area of the corresponding regular polygon, A_k^0 , where:

$$A_k = \frac{\langle \text{Area}(k) \rangle}{(r_{\text{SiSi}}^0)^2}, \quad (1.4)$$

$$A_k^0 = \frac{k}{4 \tan(\pi/k)}. \quad (1.5)$$

As the regular polygon has the maximum achievable area for a given ring size, the ratio A_k/A_k^0 is expected to lie in the range $0 \rightarrow 1$, with a lower value corresponding to increased deviation from regularity, and assuming r_{SiSi}^0 to be fixed.

The study by Kumar *et al.* found that whereas for experimental configurations, $A_k/A_k^0 \approx 1$, configurations generated using thier bond switching method generally displayed ratios much less than unity [104], indicative of large distortions in the ring structure. For larger rings, a value of $A_k/A_k^0 > 1$ was also found, which can only be achieved if there is appreciable bond stretching (see equations (??), (??)).

The analogous results for the method presented in this chapter can be found in figure ??, for $T = 10^{-3}$. This figure demonstrates that there is now good agreement between experimental and computational results. In both cases the deviation from regularity increases with ring size, as the flexibility of the rings

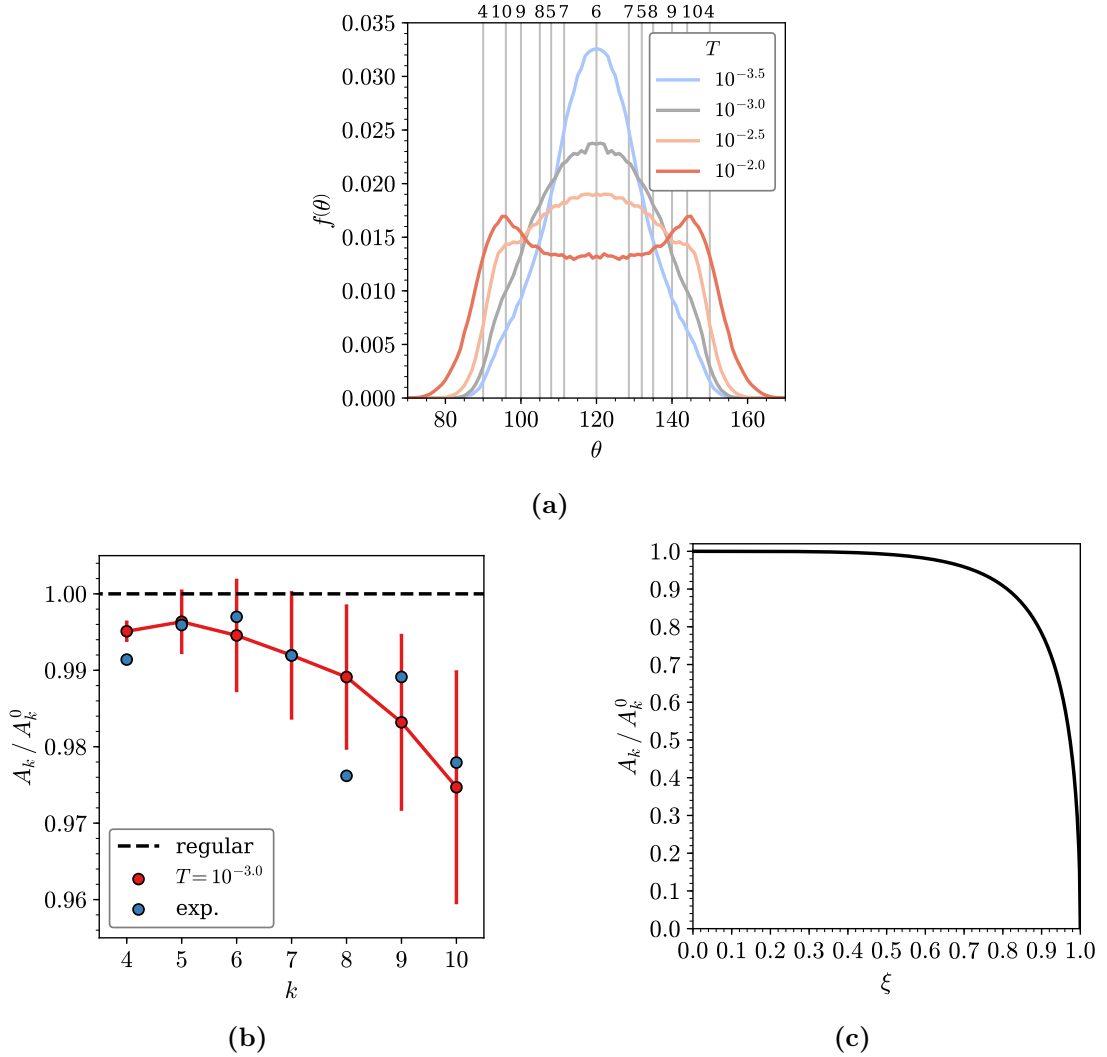


Figure 1.8: Panel (a) gives the ring angle distribution function for triangle rafts formed at different temperatures. Panel (b) compares the regularity of rings in computational and experimental amorphous configurations, with points indicating the mean value and bars corresponding to the standard deviation. Experimental data is taken from ref. [29]. Panel (c) shows the effect on the area when distorting a circle to an ellipse whilst maintaining a constant perimeter length.

increases. Again it can be proposed that the difference between current and previous methods could be due to the lack of enforced periodicity on the system. By allowing the network to grow relatively freely, the system can avoid a build up of strain associated with maintaining periodic boundaries.

Even with this analysis, an argument can be made that by visual inspection the rings in the experimental configurations are still more regular than those generated from computational samples. Therefore one can consider if deformation of a ring

should be expected to lead to significant reduction in area. This can be explored by considering the distortion of a circle to an ellipse. The degree of distortion can be described by the eccentricity of the ellipse,

$$\xi = \left(1 - \frac{b^2}{a^2}\right)^{1/2}, \quad (1.6)$$

where a , b are the major and minor axis radii respectively. This change in area with distortion is shown in figure ??, the calculation of which can be found in appendix ?. As can be seen, a large degree of eccentricity is needed for a significant change in the observable area. For example, if $a = 1.5b$, the area is still $\approx 0.94\%$ of the area of the corresponding circle.

For silica networks the Si-Si distances lie in a narrow range because of the covalent nature of the atomic bonding and the near-linear Si-O-Si bridges which join the two layers. Hence we would expect similar behaviour to occur, with ring areas relatively invariant to distortions in the ring shape (this same analysis would not be expected to hold for foams for example, where the length of the boundary is much more flexible). This suggests that the ring area is not the most suitable metric for quantifying the regularity of rings in systems such as this, and could explain any disagreement between the seemingly near ideal ring areas and the visual evidence. As previously stated, although the potential model used is physically motivated, it is lightweight in order to facilitate generation of a large number of configurations with the correct network topology. In future it would be informative to see if the required regularity can be achieved by geometry optimising the resulting bilayer configurations with a more accurate potential, such as the TS potential which includes potentially significant electrostatic interactions including many-body polarisation effects [134].

1.5 Chapter Conclusions

A method has been developed for effective modelling of silica bilayers and related materials. Bilayers are represented as triangle rafts, which are sequentially constructed from a seed using a stochastic growth algorithm. The algorithm is flexible,

allowing control over the ring size distribution and overall system topology. The success of triangle rafts in modelling silica bilayers has been demonstrated by the values of the Aboav-Weaire parameter, α , which are more commensurate with those obtained from experimental imaging than configurations generated by previous methods. Moreover, consideration of the ring areas shows that triangle raft configurations contain highly regular polygons - another experimental observation that has proved challenging to previously capture.

The real advantage of the method is that it enables a computationally tractable and systematic exploration of bilayer systems at increasing levels of disorder. This has been employed in this chapter for a detailed analysis of Lemaître's law, which rationalised why the fraction of six-membered rings observed in real systems is often ≈ 0.4 . However, it will also be used in chapter ?? to investigate the use of persistent homology in amorphous materials. The ability to build a triangle raft from any user-defined starting seed also opens further possibilities for the method. In particular, it would be interesting to see how network growth is affected by the presence of a template, which could be for example a very large ring. This could lead to insight into how to control pore geometries in these materials.

2 | Targeted Optimisation of Atomic Networks

A targeted optimisation method is presented which enables two-dimensional networks to be constructed by reference to a set of ring statistics and Aboav-Weaire parameter, α , which controls the preferred nearest-neighbour spatial correlations. The method efficiently utilises the dual lattice and allows systematic exploration of configurational space. Three different systems are considered; a system containing 5-, 6- and 7-membered rings only (a proxy for amorphous graphene), the configuration proposed by Zachariasen, and those observed experimentally for ultra-thin films of SiO_2 . The system energies are investigated as a function of the network topologies and the range of physically-realisable structures established and compared to known experimental results. The limits on α are evaluated, whilst the evolution of the network structure as a function of topology is discussed in terms of the ring-ring pair distribution functions. A short study on ring percolation in amorphous graphene is also presented.

2.1 Disorder in Two-Dimensional Networks

A central theme in this thesis is that the characterisation of the disorder in two-dimensional networks can be achieved through the ring structure. For three-coordinate atomic materials the mean ring size is constrained to six by Euler's law, which allows the variance of the ring size distribution, μ_2 , to act as a proxy measure for disorder (see sections ??, ??). The same set of ring statistics can however lead to a large number of different ring arrangements, as shown in figure ??. These can be further quantified by the Aboav-Weaire parameter, which measures the ring-ring correlations. An interesting observation across a wide range of experimental systems, is that the measured value of the Aboav-Weaire parameter lies in a tight range

of $\alpha \approx 0.15 \rightarrow 0.3$ [135]. This is also effect is also seen in computational studies, including for example the previous chapter.

Whilst it is necessary for good computational models to capture these measures accurately, they do not give insight into *why* such configurations are preferred. To answer this question a different approach is required, where configurations can be systematically generated, covering a parameter space which extends beyond the experimentally accessible region. To achieve this a targeted optimisation method can be employed, whereby configurations are produced to fit network properties, and not driven by an underlying potential model. This allows the experimentally occurring structures to be viewed in the context of the wider configurational landscape.

2.2 Targeted Optimisation Algorithm

The primary remit of the targeted optimisation algorithm is to generate plausible network configurations based on the supplied network properties of ring statistics and Aboav-Weaire parameter. A secondary requirement is for the method to be efficient enough to produce samples for further high-throughput calculations. Both these goals can be successfully accomplished with the method presented here: a Monte Carlo search algorithm, using the machinery of bond switching.

The bond switching algorithm (described in detail in section ??), amorphises a crystalline hexagonal lattice by exchanging the neighbouring interactions between pairs of bonded atoms and geometry optimising the structure. Moves are accepted according to the resulting change in the potential energy, where those with lower energy are accepted with increasing probability. The driving force is therefore always towards a structure which is physically motivated. In targeted optimisation, the same Monte Carlo moves are proposed as in bond switching, but crucially moves are not accepted on the basis of the energy of the network, but rather its agreement with a target ring distribution and Aboav-Weaire parameter. This agreement is measured by a cost function of the form:

$$\Omega = K_{\alpha} |\alpha - \alpha^t| + \frac{|\mu_2 - \mu_2^t|}{\mu_2^t} + \sum_k \frac{|p_k - p_k^t|}{p_k^t}, \quad (2.1)$$

where K_α is a scaling constant; p_k^t , μ_2^t and α^t are the input target values; p_k are the system ring statistics; and μ_2 and α are calculated from an Aboav-Weaire fit on the current state. In the cost function the relative difference is used for the ring distribution, as the same accuracy is required for all p_k^t , which may differ by several orders of magnitude. This is not a concern for α^t , which must also have the flexibility to take a zero value, and hence the absolute difference is used in the first term.

Moves in targeted optimisation are accepted with probability given by the Metropolis condition:

$$P_{ij} = \min [1, \exp -\Delta\Omega/T] , \quad (2.2)$$

where $\Delta\Omega$ is the difference in cost functions before and after the proposed move, and T is a temperature parameter. In contrast to bond switching which is concerned with sampling, this is a global optimisation algorithm and moves are proposed until the network has converged to the target properties and the cost function is zero. As is the case with such optimisation techniques, steps must be taken to avoid becoming trapped in local minima, and the calculation not converging. This is achieved through selection of the parameters K_α and T . The parameter K_α changes the relative costs of satisfying the α^t and p_k^t conditions, and must be chosen so that neither is overweighted. The parameter T controls the proportion of moves which are accepted. Some temperature is required to overcome local minima, but if set too high the algorithm will no longer move downhill in cost and the search becomes effectively random - invariably leading to non-convergence. Values for K_α and T can be determined from a parameter search checking for convergence of target systems; but $K_\alpha = 10$ and $T \sim 10^{-4}$ were appropriate for systems of the type and size described in this work.

One key point which arises from using a cost function in this way is that there becomes no requirement for accurate on-the-fly geometry optimisation of the atomic positions (as there is no need to calculate potential energies). It is the underlying topology of the network which determines the system properties, which is invariant to the geometry. The final energy of the system may well be of interest, but this

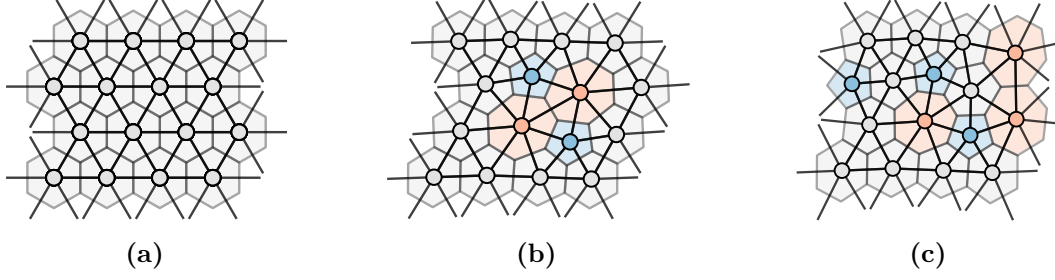


Figure 2.1: Bond switching Monte Carlo moves can be performed solely through the dual lattice. Two successive moves are shown from (a)-(b) and (b)-(c). In the dual lattice (bold circles and lines) two edge-sharing triangles are selected and the shared edge transposed. The atomic network is also shown (faded rings) to illustrate the corresponding effect on the atomic structure.

can be evaluated just once at the end of the calculation. This opens the door for significant speed-ups through efficient use of the dual lattice.

2.2.1 Dual Space Implementation

Whilst the targeted optimisation algorithm can be employed using atomic positions, there are significant advantages to a dual space implementation. As discussed in section ??, the ring structure is better described through the use of the dual network. In this representation the ring statistics in equation (1.1) are simply given by the node degree distribution. In addition, the mean ring sizes about each ring, m_j , required for the Aboav-Weaire fit, equation (??), can be easily calculated from the joint degree distribution:

$$m_j = \sum_k \frac{ke_{jk}}{q_j}. \quad (2.3)$$

Hence, by utilising the ring network, the book-keeping to track the network properties is greatly simplified.

The implementation of the bond switching move itself is also straightforward in dual space. Figure 1.1 shows how an atomic system can be manipulated *solely* through the dual lattice. Here the triangular nature of the dual (reflecting the trivalency of the atoms) can be exploited to good effect. By selecting edge sharing triangles in the ring network and transposing the shared edge connection, a perturbation equivalent to the Stone-Wales defect can be enacted. This process can be continued to generate an amorphous network.

In addition, although there is no strict requirement for geometry optimisation after each step, the triangle lattice can be used to maintain a reasonable physical structure in a cost efficient manner. By applying a harmonic potential, equation (??), between all pairs of linked nodes the ring centroids can be maintained at a reasonable separation. The atomic positions can then be regenerated by reversing the triangulation, placing species at the centre of each triangle, relatively close to the minimum in the atomic potential energy surface. Specifically, in this chapter a Keating potential, equation (??), is used with an interatomic separation of r_0 and $K_S = 5K_A$ (as in previous studies of amorphous graphene [104]). If the resultant polygons are assumed to be regular, the equilibrium separation for two polygons in the dual of sizes, k_i and k_j , can be expressed:

$$r_{ij}^0 = \frac{r_0}{2} \left(\frac{1}{\tan(\pi/k_i)} + \frac{1}{\tan(\pi/k_j)} \right). \quad (2.4)$$

The extreme computational efficiency of evaluating the forces of the harmonic potential enables the targeted optimisation algorithm to complete rapidly whilst retaining the essential physics of the system. The final geometry can then be refined.

2.3 Mapping Configurational Space

The targeted optimisation algorithm provides a opportunity to gain insight into the physical meaning of the Aboav-Weaire and its effect on network topology. For this, a variety of test systems are used, the principle of which contains only $5 \rightarrow 7$ membered rings, a proxy for amorphous graphene, aG. This system represents a useful framework for investigating the Aboav-Weaire law due to the presence of additional constraints which make it highly controllable. As a consequence of Euler's law the proportion of 5- and 7- rings must be equal, which leads to a trivial relationship between the second moment and proportion of 6- rings,

$$p_5 = p_7 = \frac{1}{2} (1 - p_6), \quad \mu_2 = 1 - p_6. \quad (2.5)$$

In addition, this allows the α parameter to be explicitly defined in terms of the difference between the 5 – 5 and 5 – 7 ring adjacencies:

$$\alpha = \frac{12\chi_{75}^5 - (1 - p_6)^2}{6(1 - p_6)}, \quad (2.6)$$

where $\chi_{75}^5 = e_{57} - e_{55}$ (details of the derivation can be found in appendix ??). This makes the aG model the first example of a system where the α parameter is well defined in terms of the underlying ring structure. It also highlights the relative complexity in the Aboav-Weaire parameter for even a seemingly simple case.

Two further systems with fixed ring statistics are also used to provide supplementary results. These are based on the Zachariasen configuration, figure ??, and experimental samples of silica glass, which are chosen to provide examples of increasing ring diversity, with the Zachariasen sample containing ring sizes in the range $k = 4 \rightarrow 8$ and silica $k = 4 \rightarrow 10$. The ring distributions for all the systems used in this chapter are summarised in table 1.1. In addition whereas the silica distribution should be easily achievable by the targeted optimisation algorithm (essentially following Lemaître’s maximum entropy distribution), the Zachariasen distribution provides a more “extreme” case, where the distribution is not unimodal and the proportion of 5-rings is greatest.

Table 2.1: Ring statistics for systems used with the targeted optimisation algorithm.

	p_4	p_5	p_6	p_7	p_8	p_9	p_{10}
aG	-	$(1 - p_6) / 2$	p_6	$(1 - p_6) / 2$	-	-	-
Zach.	0.10	0.35	0.15	0.25	0.15	-	-
SiO ₂	0.040	0.268	0.420	0.210	0.050	0.010	0.002

2.3.1 Limits of the Aboav-Weaire Parameter

To begin mapping the configurational space of these atomic networks, the range of accessible α values for the aG system was determined by generating periodic networks containing 10,000 rings with $0.1 \leq p_6 \leq 0.9$. The aim of these simulations was to try and probe the topological limits of α , and so a high number of Monte Carlo steps was used, 10^9 , without the need for geometry optimisation. Visualisations of the output of the targeted optimisation algorithm are given in figure 1.2 for $p_6 = 0.4$ and $\alpha = -0.3 \rightarrow 0.3$. These images give a good qualitative feel for the physical meaning of the Aboav-Weaire parameter: at low α similar sized rings tightly cluster together, dispersing as α increases to favour dissimilar ring pairings. Figure 1.3

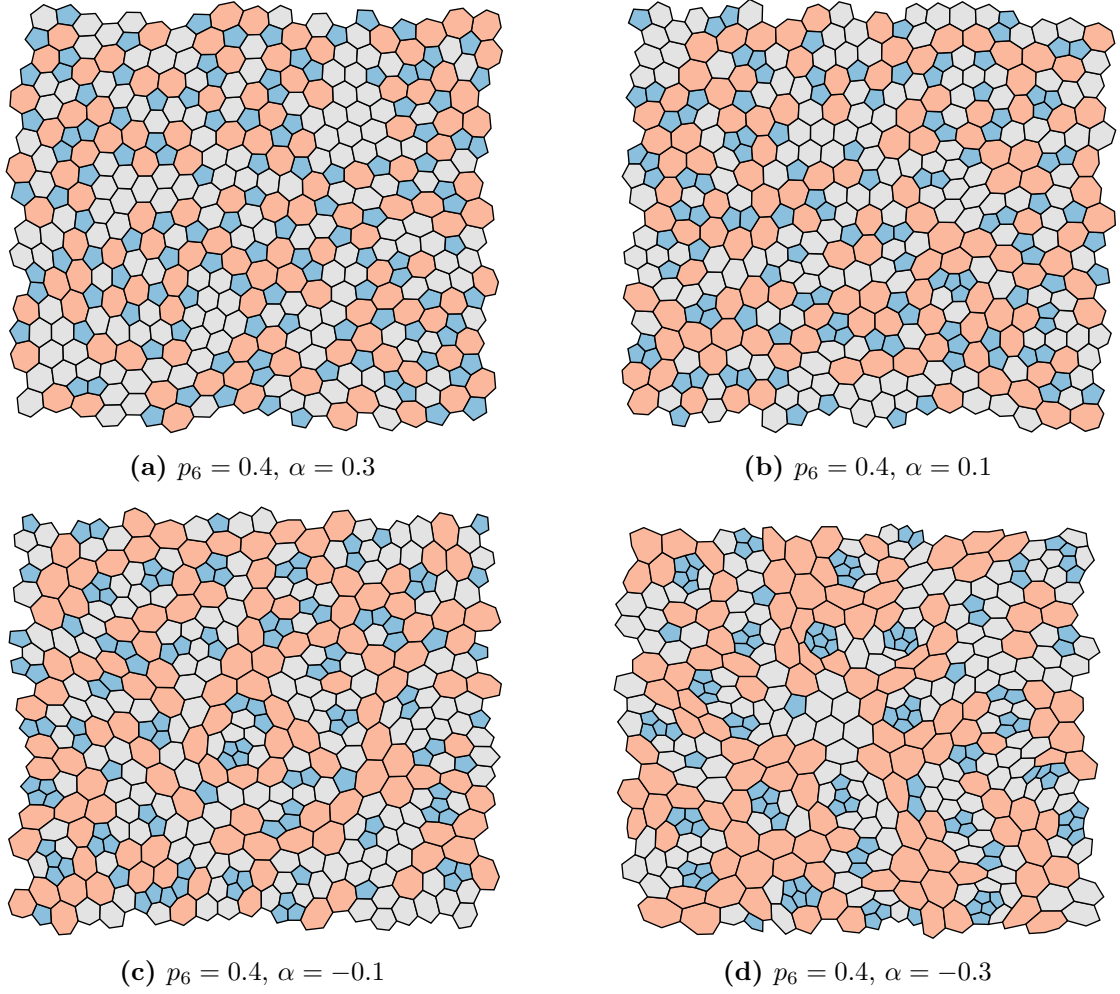


Figure 2.2: Configurations produced via targeted optimisation of an aG network with 400 rings. Each has the same ring statistics ($p_5 = 0.3$, $p_6 = 0.4$, $p_7 = 0.3$) but a variable α parameter.

shows the range of accessible α values as a function of p_6 *i.e.* those for which the targeted optimisation algorithm converges. The upper limit, α_{\max} , appears a relatively weak function of p_6 whilst the lower limit, α_{\min} , shows a much stronger dependence. In addition, the range of accessible values, $\Delta\alpha = \alpha_{\max} - \alpha_{\min}$, broadly mirrors the system entropy, although there is deviation around $p_6 = 1/3$.

2.3.2 Structure and Energetics

To explore the structural properties of the aG networks at different values of p_6 and α , 100 periodic networks containing 10,000 rings, were constructed for $p_6 = 0.2, 0.4, 0.6, 0.8$. These simulations were performed with geometry optimisation

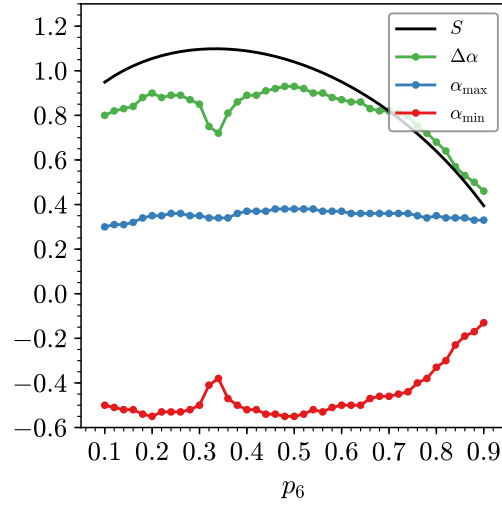


Figure 2.3: Accessible range of the Aboav-Weaire parameter in the aG system, for variable p_6 .

and so also provide information on the physical limits on α . Figure 1.4a displays the mean and standard deviation of the total potential energy for each p_6 atomic network across a range of α values. It can be seen that the energy minimum in each case is only weakly dependent on the value of p_6 , varying from $\alpha \simeq 0.23$ at $p_6 = 0.8$ to $\alpha \simeq 0.27$ at $p_6 = 0.2$, and close to the value of α seen across many natural systems. Whilst there is little cost for small deviations from the minimum, decreasing α rapidly incurs a relatively large energetic penalty. Figure 1.4b shows the analogous energies when minimising through the dual lattice alone. The curves have a very similar form with the minima aligned, suggesting that working in dual-space can be sufficient to capture all system properties, with a much lower computational overhead.

Partial radial distribution functions (RDF) can be used to further quantify any ordering imposed on the generated configurations (see section ??). These partial RDFs are constructed in reference to the distance of the centroids of a k -ring from a central j -ring, denoted $g_{jk}(r)$. They can therefore equivalently be thought of as the dual-space RDFs between nodes of degrees j, k . The Euclidean distance is used as opposed to the topological distance (*i.e.* the number of links from a given node) as the latter has been shown to lead to artificial long range correlations [136].

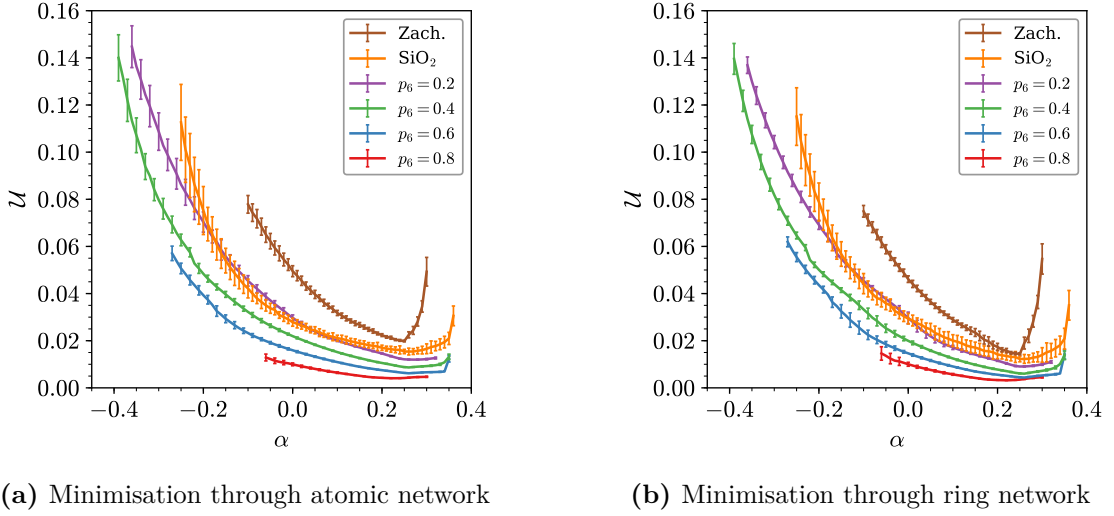


Figure 2.4: Geometry optimised potential energy of configurations produced via targeted optimisation for a range of systems with variable α parameter, with bars indicating one standard deviation from the mean. Panel (a) gives the results of optimisation through the atomic network with the Keating potential, whilst panel (b) gives the optimisation through the ring network with a simple harmonic potential.

Figures 1.5a and 1.5b show the partial RDFs for the 5-5 and 5-7 ring pairings, $g_{55}(r)$ and $g_{57}(r)$ respectively. As is consistent with its intuitive meaning, increasing α causes a reduction in intensity in the first peak of $g_{55}(r)$ and a concomitant increase in intensity in the first peak of $g_{57}(r)$, as 5-5 adjacencies are replaced with 5-7. In addition, the position of the first peak shifts to smaller r as α is reduced, reflecting both the increased distortion in the rings and the deviation from the ideal $2\pi/3$ bond angle, which translates to the higher observed potential energy.

These figures also show significant structural evolution beyond the nearest-neighbour length scale. As α becomes more positive, peaks emerge in $g_{55}(r)$ at $r/r_{55}^0 \sim 1.8$ and ~ 2.3 . An increase in α corresponds to a greater tendency for 7-rings to be near-neighbours to 5-rings and, in turn, increases the probability of the same 7-ring having a second 5-ring near-neighbour. In simple geometric terms, the second 5-ring can occupy three possible sites around the 7-ring [fig here maybe, and for 8-4-8](#), the non-adjacent positions corresponding to the developing peaks. Note that one might naïvely assume that driving α to more positive values would tend to eliminate the nearest-neighbour 5-5 spatial correlations. However, figure 1.5a indicates this not

to be the case, reflecting the balance between retaining these units and facilitating nearest-neighbour 5-7 ring interactions via the formation of 5-7-5 triplets.

Similar analysis was performed on 100 generated Zachariasen and SiO_2 networks. Although our algorithm requires the fit to equation (??) to be exactly linear for the aG system, for broader ring distributions this is no longer the case. However, for the Zachariasen configuration the linear regression (R^2) coefficient was always in excess of 0.995, and for the silica the average R^2 was 0.979, representing a very good fit. Figure 1.4a shows the energies of both the Zachariasen and SiO_2 systems as a function of α . Both cases resemble those for the aG with energy minima at $\alpha \sim 0.25$. The silica curve shows smaller curvature reflecting the broader distribution of ring sizes whilst the Zachariasen curve shows a greater curvature reflecting the “extreme” *i.e.* physically unrealistic) nature of the distribution. In addition it proved difficult to generate low α configurations ($\alpha < -0.1$) for the Zachariasen network.

Figures 1.5c and 1.5d show two key RDFs for the Zachariasen configuration, $g_{44}(r)$ and $g_{88}(r)$, highlighting the spatial correlations between the smallest and largest rings in the system. The effects of changing α on $g_{44}(r)$ are dramatic with strong nearest-neighbour clustering at negative values. In this case, however, the nearest-neighbour 4-4 correlations do vanish at high α as 4-8 nearest-neighbour correlations dominate but the 8-ring is large enough to accommodate up to four 4-ring nearest-neighbours without any 4-4 neighbouring pairs. Again this is demonstrated through the next nearest neighbours by the 8-4-8 peak developing at ~ 1.4 .

2.4 Ring Percolation in Amorphous Graphene

As a further demonstration of the utility and scope of the targeted optimisation algorithm, a short study is presented on the percolation of different ring sizes in aG systems. Owing to the fact that this is a standalone section, the theory pertinent to this investigation is first presented, followed by results.

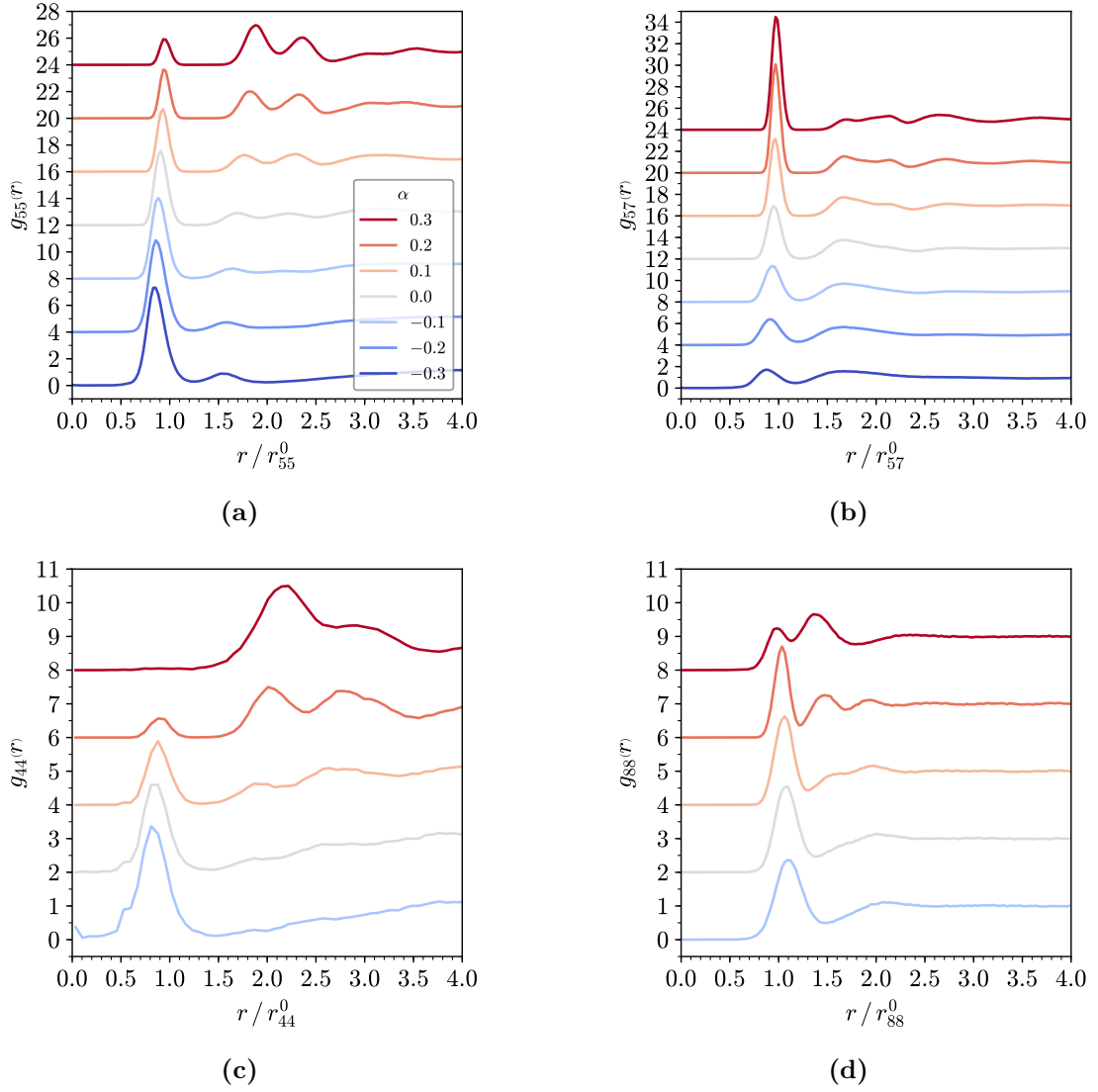


Figure 2.5: Partial RDFs for the aG (a)-(b) and Zachariasen (c)-(d) systems illustrate the evolution in ring structure with varying α parameter.

2.4.1 Percolation Theory and Clustering

Percolation theory has its roots in problems concerning the flow of fluids through porous media [137], but now it can more generally be thought of as relating to the connectedness of components in a network (also referred to as *robustness*) [138]. The theory of clustering and percolation is an extremely rich field, which this thesis will merely dip its toe into, and so the discussion of the underlying theory be framed in the context of the aG networks already introduced in this chapter.

As an introductory example, consider a pristine hexagonal lattice for which the

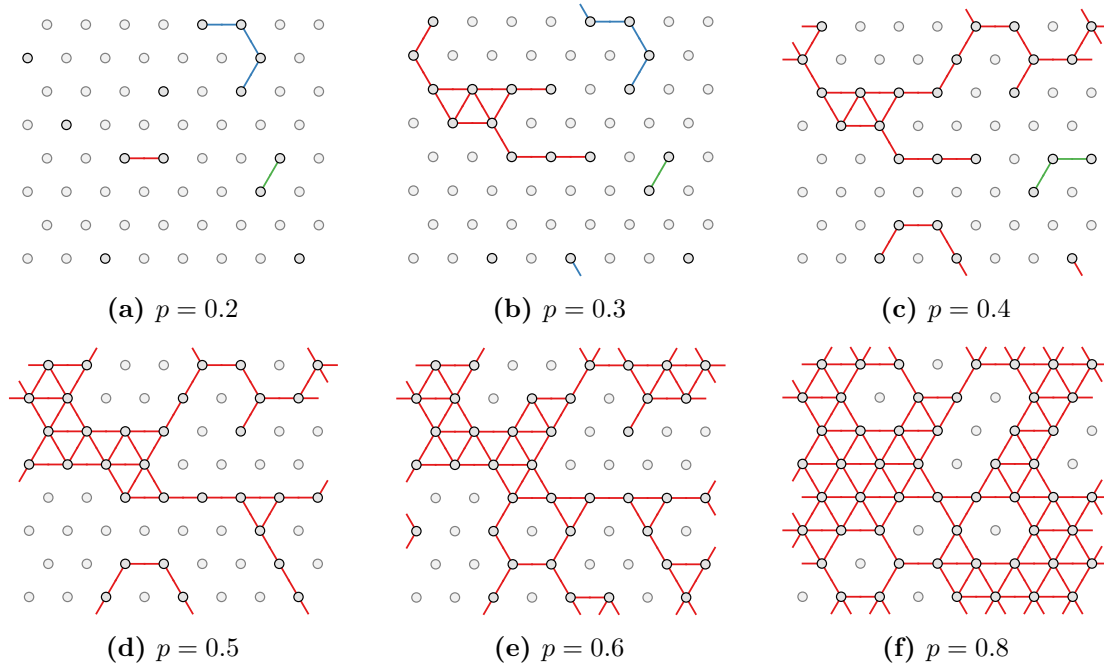


Figure 2.6: Site percolation on a triangular lattice. Panels (a)-(f) show network structure as site occupancy is increased, as indicated in the captions. Full circles signify occupied sites whilst connections are given by coloured lines, with the colour indicating nodes forming part of the same cluster.

dual structure is a triangular net. It is clear that in this lattice all the nodes are connected *i.e.* there is some continuous path linking any two given rings. Equally, one could say that all the rings belong to the same cluster. Now imagine the process of removing nodes sequentially and at random from the original lattice, as shown in figure 1.6. Initially, removing nodes will have little effect on the network structure, but after a sufficient number are deleted, the interconnectivity of all the nodes will likely be broken, and the original large cluster will fragment into smaller clusters. At some point, the lattice will undergo a phase transition, from one in which there is a single “giant” component to one which has many small components. Quantifying this behaviour is the essence of percolation theory - exploring this transition and determining at what point this “percolation threshold” occurs.

To formalise this slightly, take an infinite triangular lattice, of which a random proportion, p , of nodes are occupied. The size of a cluster (*i.e.* the number of nodes which comprise it) can be denoted, s . The probability of a cluster of given size being found in the lattice is then P_s , and so the probability of an infinitely sized

cluster as P_∞ [139]. The percolation threshold, p_c , is then the critical occupancy at which a giant component appears *i.e.*

$$P_\infty = \begin{cases} 1 & p \geq p_c \\ 0 & p < p_c \end{cases} . \quad (2.7)$$

Additionally, at this critical point, measures such as the average finite cluster size and correlation length diverge. For the example given above, which is the classic example of site percolation on a triangular lattice, the percolation threshold is $p_c = \frac{1}{2}$ [140].

The example of the triangular lattice above is one of the few examples of problems in percolation theory that can be solved analytically [141]. In order to find percolation thresholds for all but the simplest cases, numerical methods must be used. This problem is an ideal candidate for solution using a Monte Carlo method [142, 143]. One potential concern with a numerical method is that the lattices involved must be finite. The solution is to approximate the probability of a node residing in the infinite cluster as the probability of a node residing in the largest cluster. This is to say, if there are N nodes in the lattice and the maximum lattice size is s_{\max} , then

$$P_\infty \approx \frac{s_{\max}}{N} . \quad (2.8)$$

This expression will hold in the limit of $N \rightarrow \infty$. As will be seen in section 1.4.3, for finite size lattices this approximation leads to smoothing of the step-like nature of P_∞ . The percolation threshold in this case is then approximated by as the occupancy, p , for which $P_\infty = \frac{1}{2}$.

2.4.2 Percolation in Disordered Networks

The example of preceding section concerns site percolation on a regular lattice, where each site is equivalent. However, the ring networks of interest in this work are disordered, where sites have different node degrees (reflecting the underlying ring sizes). Disordered lattices therefore have an extra degree of complexity when compared to their ordered analogues. This allows the study of the percolation of different ring sizes in the network. To achieve this one must first construct the subgraphs for each ring size, which contain only the vertices and edges which relate

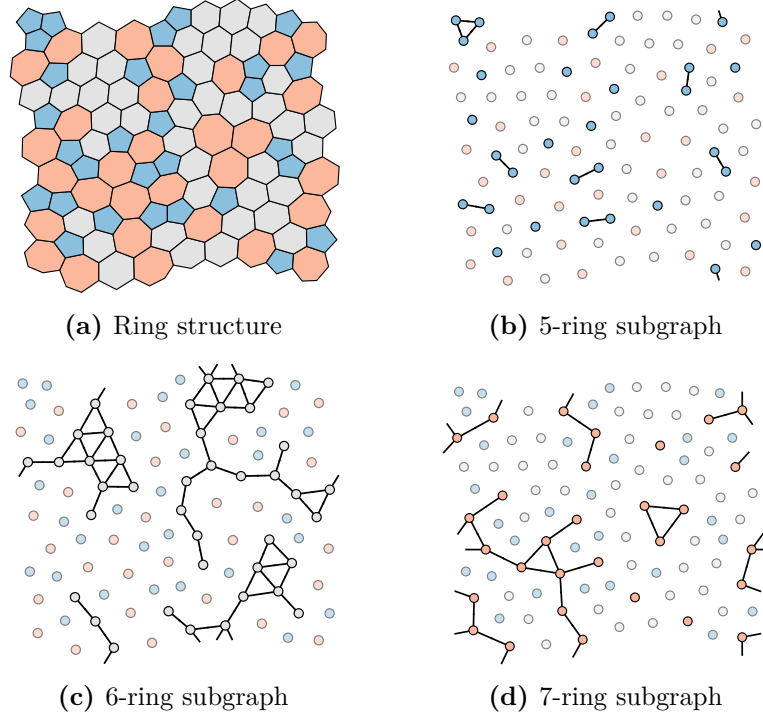


Figure 2.7: Panel (a) gives an example disordered aG ring structure and panels (b)-(e) the associated ring subgraphs, as indicated in the figure captions. Each subgraph contains only vertices and edges pertaining to the given ring size.

to a given node degree, as shown in figure 1.7. The percolation threshold can then be studied for each of these subgraphs. For each k -ring subgraph, the percolation threshold will naturally depend on the global ring statistics, p_k . However, unlike the regular lattices, the percolation threshold must also depend on the ring correlations, which must influence the clustering [144]. As seen throughout this chapter, this property is controllable through the Aboav-Weaire parameter. Therefore, for each k -ring subgraph, the percolation threshold will be a function of both a critical ring frequency, p_k^c , and a critical Aboav-Weaire value α_k^c .

2.4.3 Percolation Phase Diagram of Amorphous Graphene

The percolation phase behaviour was investigated for the aG system, containing only 5-, 6- and 7-rings. Again this system is relatively well defined in terms of the ring statistics, as shown by equation 1.5. As the accuracy of the percolation transition is dependent on the system size, very large networks were generated with 1×10^6 rings. This remained computationally tractable as the calculation of percolation

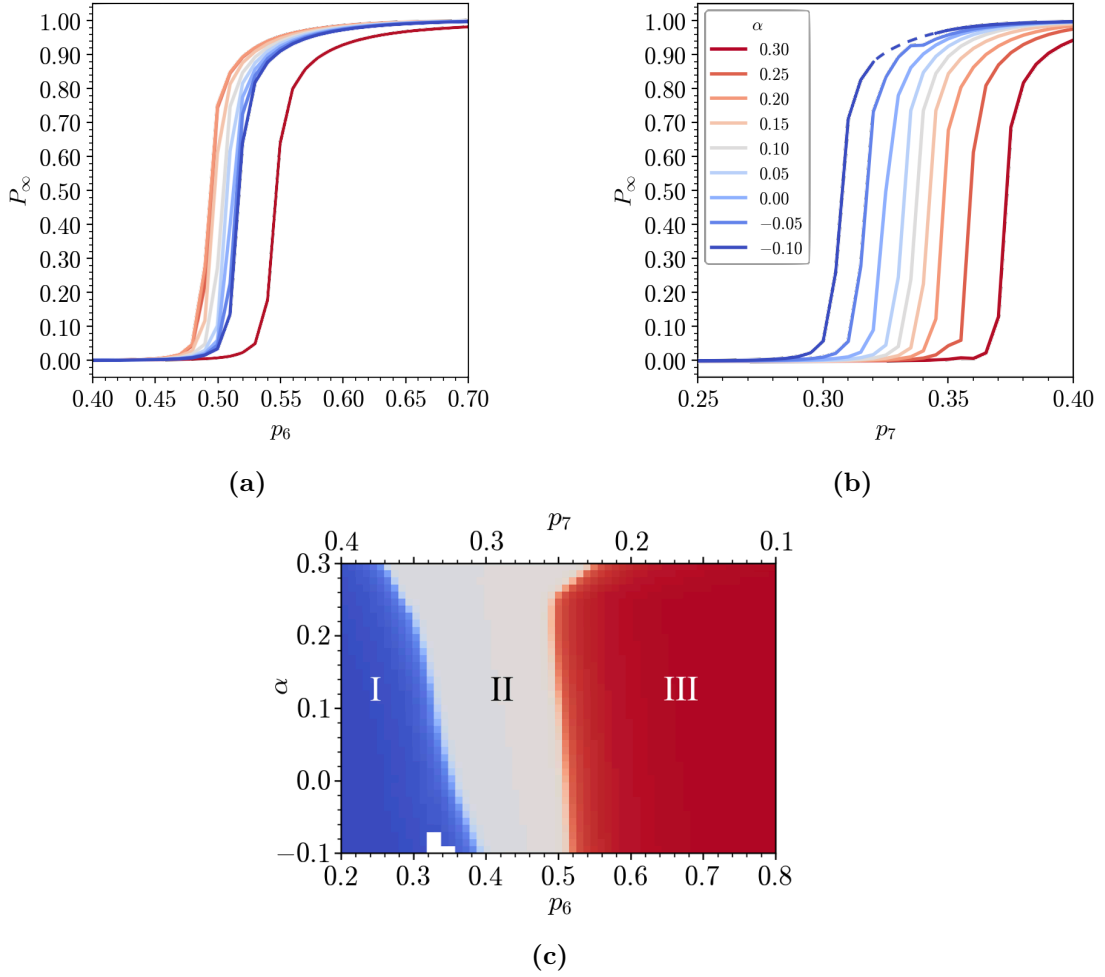


Figure 2.8: Percolation in aG configurations generated via targeted optimisation. Panels (a),(b) maps percolation as a function of α and p_6 , p_7 respectively (dashed line indicates interpolated data). The percolation threshold is defined as when $P_\infty = \frac{1}{2}$. Panel (c) gives the phase behaviour of these systems: phase I contains a giant component in the 7-ring subgraph; phase II no giant components in any subgraph; phase III a giant component in the 6-ring subgraph.

requires only the node connectivities, not their positions, and so there is no need for geometry optimisation. Networks were constructed using targeted optimisation across the full spectrum of p_6 values and with α in the range $-0.1 \rightarrow 0.3$. For each state point, 100 networks were sampled starting from different random seeds.

The results of these simulations are presented in figure 1.8. Figures 1.8a and 1.8b show the evolution in P_∞ for selected α values across the p_k range for the 6- and 7-ring subgraphs, which demonstrate slightly different behaviours. Neglecting the effect of the Aboav-Weaire parameter initially, as the proportion of a given ring

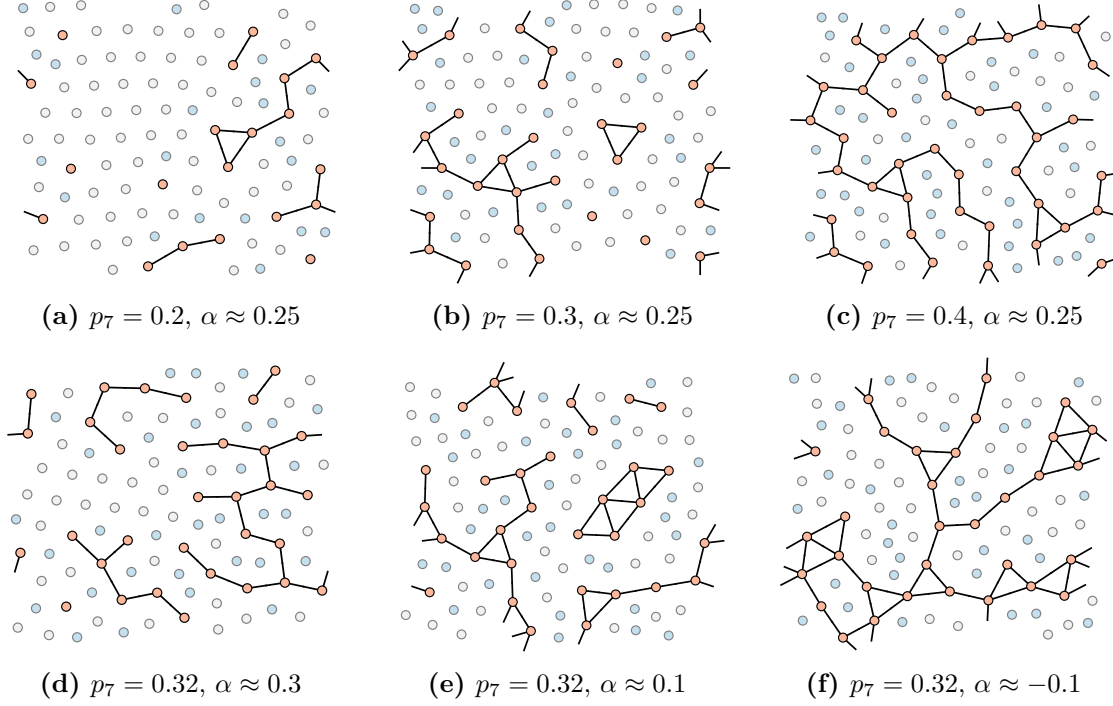


Figure 2.9: The formation of giant components in disordered networks is a function of both the proportion of each ring size (here p_7) and the ring correlations (as measured by α). Panels (a)-(c) show the effect of increasing p_7 at constant α , with a giant component only forming in (c), once a sufficient number of 7-rings are present. Conversely panels (d)-(f) show the effect of decreasing α at constant p_7 , with a giant component only forming in (f), once sufficient clustering of 7-rings is achieved.

increases, the probability of a giant component forming increases. This process is visualised in figures 1.9a-1.9c. In the case of the 6-ring subgraph, it can be seen that it bears similarity to the triangular site percolation problem discussed in section 1.4.1, with the percolation threshold oscillating around $p_6^c \approx 0.5$. The 7-ring case on the other hand displays a percolation threshold at a lower value of $p_7^c \approx 0.35$. This is intuitive as each node has a greater number of edges emanating from it, and so a greater probability of connecting to other ring sizes. It is also for this reason that there is *no* percolation threshold for the 5-ring subgraph in aG. This can be rationalised by realising that as $p_5 = p_7$, and a 7-ring by definition has more connections to adjacent rings than the 5-ring, there can never be a point where the 5-rings can form a giant component in preference to the 7-rings. In the most extreme case, one can see this in the example of haeckelite, in which $p_5 = p_7 = \frac{1}{2}$ and all 7-rings are connected, yet the 5-rings remain isolated from one another.

The behaviour of the network percolation threshold is also subtly related to the node correlations, as expected [145, 146]. For the 7-ring subgraph, the percolation threshold in p_7 systematically decreases with decreasing α . This is because a decreasing α is reflective of increased large-large ring pairings, thus facilitating the formation of a connected giant component of 7-rings. This process is demonstrated in figures 1.9d-1.9f. The 6-ring shows what appears to be a more complex relationship with α . Initially as α is increased, the percolation threshold in p_6 decreased, before suddenly increasing again at high α . This is a consequence of the fact that the 6-ring is the “middle” ring size. Hence when α is strongly negative, $7 - 6$ pairings are most favoured and when α is strongly positive $6 - 5$ pairings are more abundant. It is only when α sits in the intermediate region that the $6 - 6$ ring correlations are maximised and percolation is most readily facilitated. It is interesting to note that this also around the value of $\alpha \approx 0.25$ that is also common in nature.

The results discussed above can be combined to draw a percolation phase diagram for aG, presented in figure 1.8c. In this diagram there are three phases:

- **Phase I:** exists at low $p_6 \lesssim 0.35$ and preferentially low α , where networks contain a giant component of 7-rings
- **Phase II:** occupies intermediate values of p_6 , where no subgraph contains a giant component
- **Phase III:** encompasses the largest region of phase space, for $p_6 \gtrsim 0.5$, where networks contain a giant component of 6-rings

From this phase behaviour it can be seen that relatively low values of p_6 must be achieved before the percolation of 6-rings is broken. In addition it is unlikely that an phase I could be experimentally realised and percolation of the 7-rings achieved. This is because from maximum entropy, the most disordered lattice possible would have $p_5 = p_6 = p_7 = \frac{1}{3}$ which is on the fringe of the percolation threshold for p_7 , and would necessitate a value of α much lower than is currently seen experimentally. This could have implications when designing materials, for which there are eigenstates which are localised on specific ring sizes [147, 148].

2.5 Chapter Conclusions

An innovative method has been presented to generate two-dimensional network materials with well defined topology. This targeted Monte Carlo search algorithm allows configurations to be constructed which have precise ring size distributions and ring-ring correlations. The advantage of this approach is that configurations can be produced rapidly with controllable properties; which may lie outside experimentally or physically accessible regions of phase space. These configurations may then be used as starting points for further investigations. For example, the algorithm outlined in this work has already been utilised to study the mechanical properties of vitreous silica under deformation [149, 150]. In this chapter the targeted optimisation method was employed to probe the physical meaning of the Aboav-Weaire parameter. The effect of α on the ring structure has been quantified through partial RDFs, and the energetic minima for a range of systems has been shown to correspond well with values commonly found in nature. Finally, the method was employed in a study of the ring percolation in amorphous graphene, with the phase behaviour quantified in terms of the ring statistics and the Aboav-Weaire parameter.

Appendices

References

- [1] W H Zachariasen. “The Atomic Arrangement in Glass”. In: *J. Am. Chem. Soc.* 54.10 (1932), pp. 3841–3851.
- [2] J. Kotakoski et al. “From point defects in graphene to two-dimensional amorphous carbon”. In: *Phys. Rev. Lett.* 106 (2011), p. 105505.
- [3] Alex W. Robertson et al. “Spatial control of defect creation in graphene at the nanoscale”. In: *Nat. Commun.* 3 (2012), p. 1144.
- [4] Pinshane Y Huang et al. “Direct Imaging of the a Two-Dimensional Silica Glass on Graphene”. In: *Nano Lett.* 12 (2012), pp. 1081–1086.
- [5] Leonid Lichtenstein, Markus Heyde, and Hans Joachim Freund. “Atomic arrangement in two-dimensional silica: From crystalline to vitreous structures”. In: *J. Phys. Chem. C* 116 (2012), pp. 20426–20432.
- [6] Shamil Shaikhutdinov and Hans-joachim Freund. “Metal-Supported Aluminosilicate Ultrathin Films as a Versatile Tool for Studying the Surface Chemistry of Zeolites”. In: *ChemPhysChem* 14 (2013), pp. 71–77.
- [7] Adrián Leandro Lewandowski et al. “Atomic structure of a metal-supported two-dimensional germania film”. In: *Phys. Rev. B* 97 (2018), p. 115406.
- [8] L Lewandowski et al. “From Crystalline to Amorphous Germanium Bilayer Films at the Atomic Scale: Preparation and Characterization”. In: *Angew. Chem. Int. Ed.* 58 (2019), pp. 10903–10908.
- [9] Panagiotis Trogadas, Thomas F Fuller, and Peter Strasser. “Carbon as catalyst and support for electrochemical energy conversion”. In: *Carbon N. Y.* 75 (2014), pp. 5–42.
- [10] Yongfu Sun et al. “Ultrathin Two-Dimensional Inorganic Materials : New Opportunities for Solid State Nanochemistry”. In: *Acc. Chem. Res.* 48 (2015), pp. 3–12.
- [11] Christin Büchner and Markus Heyde. “Two-dimensional silica opens new perspectives”. In: *Prog. Surf. Sci.* 92 (2017), pp. 341–374.
- [12] Paul A Beck. “Annealing of cold worked metals”. In: *Adv. Phys.* 3.11 (1954), pp. 245–324.
- [13] C G Dunn and E F Koch. “Comparison of Dislocation Densities of Primary and Secondary Recrystallization Grains of Si-Fe”. In: *Acta Metall.* 5 (1957), p. 548.
- [14] A J Stone and D J Wales. “Theoretical Studies of Icosahedra C60 and Some Related Species”. In: *Chem. Phys. Lett.* 128.5,6 (1986), pp. 501–503.

- [15] J. Shackelford and B. D. Brown. “The Lognormal Distribution in the Random Network Structure”. In: *J. Non. Cryst. Solids* 44 (1981), pp. 379–382.
- [16] J Lemaitre et al. “Arrangement of cells in Voronoi tessellations of monosize packing of discs”. In: *Philos. Mag. B* 67.3 (1993), pp. 347–362.
- [17] Leonid Lichtenstein et al. “The atomic structure of a metal-supported vitreous thin silica film”. In: *Angew. Chemie - Int. Ed.* 51 (2012), pp. 404–407.
- [18] D A Aboav. “Arrangement of grains in a polycrystal”. In: *Metallography* 3 (1970), pp. 383–390.
- [19] D. Weaire. “Some remarks on the arrangement of grains in a polycrystal”. In: *Metallography* 7 (1974), pp. 157–160.
- [20] Torbjörn Björkman et al. “Defects in bilayer silica and graphene: Common trends in diverse hexagonal two-dimensional systems”. In: *Sci. Rep.* 3 (2013), p. 3482.
- [21] Andrei Malashevich, Sohrab Ismail-Beigi, and Eric I. Altman. “Directing the structure of two-dimensional silica and silicates”. In: *J. Phys. Chem. C* 120 (2016), pp. 26770–26781.
- [22] Mark Wilson et al. “Modeling vitreous silica bilayers”. In: *Phys. Rev. B* 87 (2013), p. 214108.
- [23] Mark Wilson and Harry Jenkins. “Crystalline thin films of silica : modelling , structure and energetics”. In: *J. Phys. Condens. Matter* 30 (2018), p. 475401.
- [24] Jin Zhang. “Phase-dependent mechanical properties of two-dimensional silica films: A molecular dynamics study”. In: *Comput. Mater. Sci.* 142 (2018), pp. 7–13.
- [25] Franz Bamer, Firaz Ebrahim, and Bernd Markert. “Athermal mechanical analysis of Stone-Wales defects in two-dimensional silica”. In: *Comput. Mater. Sci.* 163 (2019), pp. 301–307.
- [26] Projesh Kumar Roy and Andreas Heuer. “Ring Statistics in 2D Silica: Effective Temperatures in Equilibrium”. In: *Phys. Rev. Lett.* 122 (2019), p. 016104.
- [27] Nina F. Richter et al. “Characterization of Phonon Vibrations of Silica Bilayer Films”. In: *J. Phys. Chem. C* 123 (2019), pp. 7110–7117.
- [28] Projesh Kumar Roy, Markus Heyde, and Andreas Heuer. “Modelling the atomic arrangement of amorphous 2D silica: a network analysis”. In: *Phys. Chem. Chem. Phys.* 20 (2018), pp. 14725–14739.
- [29] Avishek Kumar et al. “Ring statistics of silica bilayers”. In: *J. Phys. Condens. Matter* 26 (2014), p. 395401.
- [30] D. A. Aboav. “The arrangement of cells in a net. I”. In: *Metallography* 13 (1980), pp. 43–58.
- [31] B. N. Boots. “Comments on "Aboav’s Rule" for the Arrangement of Cells in a Network”. In: *Metallography* 17 (1984), pp. 411–418.
- [32] J. C. Earnshaw and D. J. Robinson. “Topological correlations in colloidal aggregation”. In: *Phys. Rev. Lett.* 72.23 (1994), p. 3682.
- [33] C Allain and L Limat. “Regular Patterns of Cracks Formed by Directional Drying of a Colloidal Suspension”. In: *Phys. Rev. Lett.* 74.15 (1995), p. 2981.

- [34] A Moncho-Jorda, F Martinez-Lopez, and R Hidalgo-Alvarez. “Simulations of aggregation in 2D . A study of kinetics , structure and topological properties”. In: *Physica A* 282 (2000), pp. 50–64.
- [35] Marc Durand et al. “Statistical mechanics of two-dimensional shuffled foams: Prediction of the correlation between geometry and topology”. In: *Phys. Rev. Lett.* 107 (2011), p. 168304.
- [36] Mingming Tong et al. “Geometry and Topology of Two-Dimensional Dry Foams : Computer Simulation and Experimental Characterization”. In: *Langmuir* 33 (2017), pp. 3839–3846.
- [37] Lucas Goehring and Stephen W Morris. “Cracking mud, freezing dirt, and breaking rocks”. In: *Phys. Today* 67.11 (2014), p. 39.
- [38] D Brutin et al. “Pattern formation in drying drops of blood”. In: *J. Fluid Mech.* 667 (2011), pp. 85–95.
- [39] Franziska Glassmeier and Graham Feingold. “Network approach to patterns in stratocumulus clouds”. In: *PNAS* 114.40 (2017), pp. 10578–10583.
- [40] Michel C Milinkovitch et al. “Crocodile Head Scales Are Not Developmental Units But Emerge From Physical Cracking”. In: *Science (80-.)*. 339 (2019), pp. 78–81.
- [41] G. Le Caër and R. Delannay. “The administrative divisions of mainland France as 2D random cellular structures”. In: *J. Phys. Fr.* 3 (1993), p. 1777.
- [42] G Schliecker and S Klapp. “Why are the equilibrium properties of two-dimensional random cellular structures so similar?” In: *Europhys. Lett.* 48.2 (1999), pp. 122–128.
- [43] William T. Gibson et al. “Control of the mitotic cleavage plane by local epithelial topology”. In: *Cell* 144 (2011), pp. 427–438.
- [44] M Kokalj Ladan, P Ziherl, and A Šiber. “Topology of dividing planar tilings : Mitosis and order in epithelial tissues”. In: *Phys. Rev. E* 100 (2019), p. 012410.
- [45] D. Weaire and N. Rivier. “Soap, cells and statistics-random patterns in two dimensions”. In: *Contemp. Phys.* 50.1 (2009), pp. 199–239.
- [46] J C Flores. “Mean-field crack networks on desiccated films and their applications : Girl with a Pearl Earring”. In: *Soft Matter* 13 (2017), pp. 1352–1356.
- [47] Steven H Strogatz. “Exploring complex networks”. In: *Nature* 410 (2001), p. 268.
- [48] S Boccaletti et al. “Complex networks : Structure and dynamics”. In: *Phys. Rep.* 424 (2006), pp. 175–308.
- [49] Albert-László Barabási. “The network takeover”. In: *Nat. Phys.* 8 (2012), pp. 14–16.
- [50] Alice L. Thorneywork et al. “Two-Dimensional Melting of Colloidal Hard Spheres”. In: *Phys. Rev. Lett.* 118 (2017), p. 158001.
- [51] Andrew B Cairns et al. “Design of crystal-like aperiodic solids with selective disorder–phonon coupling”. In: *Nat. Commun.* 7 (2016), p. 10445.
- [52] Larry Wasserman. “Topological Data Analysis”. In: *Annu. Rev. Stat. Appl.* 5 (2018), p. 501.

- [53] Sheneve Z Butler et al. “Opportunities in Two-Dimensional Materials Beyond Graphene”. In: *ACS Nano* 7.4 (2013), pp. 2898–2926.
- [54] Ganesh R Bhimanapati et al. “Recent Advances in Two-Dimensional Materials beyond Graphene”. In: *ACS Nano* 9.12 (2015), pp. 11509–11539.
- [55] Chaoliang Tan et al. “Recent Advances in Ultrathin Two-Dimensional Nanomaterials”. In: *Chem. Rev.* 117 (2017), pp. 6225–6331.
- [56] Paul M Chaikin and T C Lubensky. *Principles of condensed matter physics [electronic resource]*. Cambridge core. Cambridge ; New York, NY, USA: Cambridge University Press, 1995.
- [57] Albert-László Barabási and Márton Pósfai. *Network science*. Cambridge: Cambridge University Press, 2016.
- [58] Xianglong Yuan and A N Cormack. “Efficient algorithm for primitive ring statistics in topological networks”. In: *Comput. Mater. Sci.* 24 (2002), pp. 343–360.
- [59] D. A. Aboav. “The Arrangement of Cells in a Net. III”. In: *Metallography* 17 (1984), pp. 383–396.
- [60] E Ressouche et al. “Magnetic Frustration in an Iron-Based Cairo Pentagonal Lattice”. In: *Phys. Rev. Lett.* 103 (2009), p. 267204.
- [61] P W Fowler et al. “Energetics of Fullerenes with Four-Membered Rings”. In: *J Phys Chem* 100 (1996), pp. 6984–6991.
- [62] A. Gervois, J. P. Troadec, and J. Lemaitre. “Universal properties of Voronoi tessellations of hard discs”. In: *J. Phys. A* 25 (1992), pp. 6169–6177.
- [63] G. Le Caër and R. Delannay. “Correlations in Topological Models of 2d Random Cellular Structures”. In: *J. Phys. A* 26 (1993), pp. 3931–3954.
- [64] P Cerisier, S Rahal, and N Rivier. “Topological correlations in Benard-Marangoni convective structures”. In: *Phys. Rev. E* 54.5 (1996), pp. 5086–5094.
- [65] Matthew P. Miklius and Sascha Hilgenfeldt. “Analytical results for size-topology correlations in 2D disk and cellular packings”. In: *Phys. Rev. Lett.* 108 (2012), p. 015502.
- [66] N Rivier, D Weaire, and R Romer. “Tetrahedrally Bonded Random Networks Without Odd Rings”. In: *J. Non. Cryst. Solids* 105 (1988), pp. 287–291.
- [67] F. T. Lewis. “The correlation between cell division and the shapes and sizes of prismatic cell in the epidermis of cucumis”. In: *Anat. Rec.* 38.3 (1928), pp. 341–376.
- [68] M. A. Fortes. “Applicability of the Lewis and Aboav-Weaire laws to 2D and 3D cellular structures based on Poisson partitions”. In: *J. Phys. A* 28 (1995), pp. 1055–1068.
- [69] Sangwoo Kim, Muyun Cai, and Sascha Hilgenfeldt. “Lewis’ law revisited: the role of anisotropy in size-topology correlations”. In: *New J. Phys.* 16 (2014), p. 015024.
- [70] S. N. Chiu. “Aboav-Weaire’s and Lewis’ laws - A review”. In: *Mater. Charact.* 34 (1995), pp. 149–165.

- [71] Renaud Delannay and Gérard Le Caër. “Topological characteristics of 2D cellular structures generated by fragmentation”. In: *Phys. Rev. Lett.* 73.11 (1994), pp. 1553–1556.
- [72] S Le Roux and F Rezai-Aria. “Topological and metric properties of microscopic crack patterns : application to thermal fatigue of high temperature”. In: *J. Phys. D* 46 (2013), p. 295301.
- [73] David A Noever. “Statistics of emulsion lattices”. In: *Colloids and Surfaces* 62 (1992), pp. 243–247.
- [74] J. C. M. Mombach, R. M. C. de Almeida, and J. R. Iglesias. “Two-cell correlations in biological tissues”. In: *Phys. Rev. E* 47.5 (1993), pp. 3712–3717.
- [75] P Pedro et al. “Polygonal terrains on Mars : A contribution to their geometric and topological characterization”. In: *Planet. Space Sci.* 56 (2008), pp. 1919–1924.
- [76] David P Landau and Kurt Binder. *A Guide to Monte Carlo Simulations in Statistical Physics*. 4th ed. Cambridge University Press, 2014.
- [77] David J Wales and Harold A Scheraga. “Global Optimization of Clusters, Crystals, and Biomolecules”. In: *Science (80-.)*. 285 (1999), pp. 1368–1372.
- [78] Andrea C Levi and Miroslav Kotrla. “Theory and simulation of crystal growth”. In: *J. Phys. Condens. Matter* 9 (1997), p. 299.
- [79] C Ratsch and J A Venables. “Nucleation Theory and the Early Stages of Thin Film Growth”. In: *J. Vac. Sci. Technol. A* 21 (2003), S96.
- [80] Wlaler Kob. “Computer simulations of supercooled liquids and glasses”. In: *J. Phys. Condens. Matter* 11 (1999), R85.
- [81] Pablo Jensen. “Growth of nanostructures by cluster deposition: Experiments and simple models”. In: *Rev. Mod. Phys.* 71.5 (1999), pp. 1695–1735.
- [82] Daan Frenkel and Berend Smit. *Understanding Molecular Simulation: from Algorithms to Applications*. 2nd ed. Academic Press, 2002.
- [83] M P Allen and D J Tildesley. *Computer simulation of liquids*. 2nd ed. Oxford Science Publications, 2017.
- [84] Steve Brooks et al. *Handbook of Markov Chain Monte Carlo*. CRC Press, 2011.
- [85] N Metropolis et al. “Equation of State Calculations by Fast Computing Machines”. In: *J. Chem. Phys.* 21.6 (1953), pp. 1087–1092.
- [86] Vasilios I Manousiouthakis and Michael W Deem. “Strict detailed balance is unnecessary in Monte Carlo simulation”. In: *J. Chem. Phys.* 110 (1999), p. 2753.
- [87] Hidemaro Suwa and Synge Todo. “Markov Chain Monte Carlo Method without Detailed Balance”. In: *Phys. Rev. Lett.* 105 (2010), p. 120603.
- [88] Manon Michel, Sebastian C Kapfer, and Werner Krauth. “Generalized event-chain Monte Carlo:” in: *J. Chem. Phys.* 140 (2014), p. 054116.
- [89] G M Torrie and J P Valleau. “Nonphysical Sampling Distributions in Monte Carlo Free-Energy Estimation: Umbrella Sampling”. In: *J. Comput. Phys.* 23 (1977), pp. 187–199.
- [90] David J Earl and Michael W Deem. “Parallel tempering: Theory, applications, and new perspectives”. In: *Phys. Chem. Chem. Phys.* 7 (2005), pp. 3910–3916.

- [91] Bernd Hartke. “Global Geometry Optimization of Clusters Using Genetic Algorithms”. In: *J. Phys. Chem.* 97 (1993), pp. 9973–9976.
- [92] J A Niesse and Howard R Mayne. “Global geometry optimization of atomic clusters using a modified genetic algorithm in space-fixed coordinates”. In: *J. Chem. Phys.* 105 (1996), p. 4700.
- [93] David J Wales and Jonathan P K Doye. “Global Optimization by Basin-Hopping and the Lowest Energy Structures of Lennard-Jones Clusters Containing up to 110 Atoms”. In: *J. Phys. Chem. A* 101 (1997), pp. 5111–5116.
- [94] S . Kirkpatrick, C . D . Gelatt Jr., and M . P . Vecchi. “Optimization by Simulated Annealing”. In: *Science (80-.)*. 220.4598 (1983), pp. 671–680.
- [95] Darrall Henderson, Sheldon H Jacobson, and Alan W Johnson. “The Theory and Practice of Simulated Annealing”. In: *Handb. Metaheuristics*. Ed. by Fred Glover and Gary A Kochenberger. Boston, MA: Springer US, 2003, pp. 287–319.
- [96] F Wooten, K Winer, and D Weaire. “Computer Generation of Structural Models of Amorphous Si and Ge”. In: *Phys. Rev. Lett.* 54.13 (1985), pp. 1392–1395.
- [97] M M J Treacy and K B Borisenko. “The Local Structure of Amorphous Silicon”. In: *Science (80-.)*. 335 (2012), pp. 950–953.
- [98] Yuhai Tu et al. “Properties of a Continuous-Random-Network Model for Amorphous Systems”. In: *Phys. Rev. Lett.* 81.22 (1998), pp. 4899–4902.
- [99] B R Djordjevic, M F Thorpe, and F Wooten. “Computer model of tetrahedral amorphous diamond”. In: *Phys. Rev. B* 52.8 (1995), pp. 5685–5690.
- [100] Normand Mousseau and G T Barkema. “Binary continuous random networks”. In: *J. Phys. Condens. Matter* 16 (2004), S5183–S5190. arXiv: 0408705 [cond-mat].
- [101] E M Huisman, C Storm, and G T Barkema. “Monte Carlo study of multiply crosslinked semiflexible polymer networks”. In: *Phys. Rev. E* 78 (2008), p. 051801.
- [102] C P Broedersz and F C Mackintosh. “Modeling semiflexible polymer networks”. In: *Rev. Mod. Phys.* 86 (2014), pp. 995–1036.
- [103] Sandeep K Jain and Gerard T Barkema. “Rupture of amorphous graphene via void formation”. In: *PCCP* 20 (2018), pp. 16966–16972.
- [104] Avishek Kumar, Mark Wilson, and M F Thorpe. “Amorphous graphene: a realization of Zachariasen’s glass”. In: *J. Phys. Condens. Matter* 24 (2012), p. 485003.
- [105] P. N. Keating. “Effect of invariance requirements on the elastic strain energy of crystals with application to the diamond structure”. In: *Phys. Rev.* 145.2 (1966), pp. 637–645.
- [106] G. Barkema and Normand Mousseau. “High-quality continuous random networks”. In: *Phys. Rev. B* 62.8 (2000), pp. 4985–4990.
- [107] D A Drabold. “Topics in the theory of amorphous materials”. In: *Eur Phys J B* 68 (2009), pp. 1–21.
- [108] S. von Alftan, A. Kuronen, and K. Kaski. “Realistic models of amorphous silica: A comparative study of different potentials”. In: *Phys. Rev. B* 68 (2003), p. 073203.

- [109] Monica Bulacu et al. “Improved Angle Potentials for Coarse-Grained Molecular Dynamics Simulations”. In: *J. Chem. Theory Comput.* 9 (2013), pp. 3282–3292.
- [110] Jorge Nocedal and Stephen J Wright. *Numerical Optimization*. 2nd ed. Springer, 2006.
- [111] Normand Mousseau and G. T. Barkema. “Fast bond-transposition algorithms for generating covalent amorphous structures”. In: *Curr. Opin. Solid State Mater. Sci.* 5 (2001), pp. 497–502.
- [112] Masaharu Isobe. “Hard sphere simulation in statistical physics - methodologies and applications”. In: *Mol. Simul.* 42.16 (2016), pp. 1317–1329.
- [113] Etienne P Bernard, Werner Krauth, and David B Wilson. “Event-chain Monte Carlo algorithms for hard-sphere systems”. In: *Phys. Rev. E* 80 (2009), p. 056704.
- [114] Joshua A Anderson et al. “Massively parallel Monte Carlo for many-particle simulations on GPUs”. In: *J. Comput. Phys.* 254 (2013), pp. 27–38.
- [115] Masaharu Isobe and Werner Krauth. “Hard-sphere melting and crystallization with event-chain Monte Carlo”. In: *J. Chem. Phys.* 143 (2015), p. 084509.
- [116] B Widom. “Random Sequential Addition of Hard Spheres to a Volume”. In: *J Chem Phys* 44 (1966), p. 3888.
- [117] L V Woodcock. “Glass Transition in the Hard-Sphere Model”. In: *J Chem Soc Faraday Trans 2* 72 (1976), pp. 1667–1672.
- [118] T S Grigera and G Parisi. “Fast Monte Carlo algorithm for supercooled soft spheres”. In: *Phys. Rev. E* 63 (2001), 045102(R).
- [119] Andrea Ninarello, Ludovic Berthier, and Daniele Coslovich. “Models and Algorithms for the Next Generation of Glass Transition Studies”. In: *Phys. Rev. X* 7 (2017), p. 021039.
- [120] A Okabe, B Boots, and K Sugihara. *Spatial Tessellations: Concepts and Applications of Voronoi Diagrams*. Wiley, 1992.
- [121] Anne Poupon. “Voronoi and Voronoi-related tessellations in studies of protein structure and interaction”. In: *Curr. Opin. Struct. Biol.* 14 (2004), pp. 233–241.
- [122] B. J. Gellatly and J. L. Finney. “Characterisation of Models of Multicomponent Amorphous Metals: the Radical Alternative to the Voronoi Polyhedron”. In: *J. Non. Cryst. Solids* 50 (1982), pp. 313–329.
- [123] F Aurenhammer. “Power diagrams: properties, algorithms and applications”. In: *SIAM J Comput* 16.1 (1987), pp. 78–96.
- [124] FM Richards. “The Interpretation of Protein Structures : Total Volume, Group Volume Distributions and Packing Density”. In: *J Mol Biol* 82 (1974), pp. 1–14.
- [125] Chris H Rycroft. “VORO++ : A three-dimensional Voronoi cell library in C ++”. In: *Chaos* 19 (2009), p. 041111.
- [126] B N Boots. “The Spatial Arrangement of Random Voronoi Polygons”. In: *Comput. Geosci.* 9.3 (1983), pp. 351–365.
- [127] Masaharu Tanemura. “Statistical Distributions of Poisson Voronoi Cells in Two and Three Dimensions”. In: *Forma* 18 (2003), pp. 221–247.

- [128] D. Löffler et al. “Growth and structure of crystalline silica sheet on Ru(0001)”. In: *Phys. Rev. Lett.* 105 (2010), p. 146104.
- [129] Leonid Lichtenstein, Markus Heyde, and Hans Joachim Freund. “Crystalline-vitreous interface in two dimensional silica”. In: *Phys. Rev. Lett.* 109 (2012), p. 106101.
- [130] Mahdi Sadjadi et al. “Refining glass structure in two dimensions”. In: *Phys. Rev. B* 96 (2017), 201405(R).
- [131] James F. Shackelford. “Triangle rafts - extended Zachariasen schematics for structure modeling”. In: *J. Non. Cryst. Solids* 49 (1982), pp. 19–28.
- [132] Christin Büchner et al. “Building block analysis of 2D amorphous networks reveals medium range correlation”. In: *J. Non. Cryst. Solids* 435 (2016), pp. 40–47.
- [133] Louis Theran et al. “Anchored boundary conditions for locally isostatic networks”. In: *Phys. Rev. E* 92 (2015), p. 053306.
- [134] P. Tangney and S. Scandolo. “An ab initio parametrized interatomic force field for silica”. In: *J. Chem. Phys.* 117 (2002), pp. 8898–8904.
- [135] I. Zsoldos and A. Szasz. “Appearance of collectivity in two-dimensional cellular structures”. In: *Comput. Mater. Sci.* 15 (1999), pp. 441–448.
- [136] Mahdi Sadjadi and M. F. Thorpe. “Ring correlations in random networks”. In: *Phys. Rev. E* 94 (2016), p. 062304.
- [137] S R Broadbent and J M Hammersley. “Percolation processes I. Crystals and Mazes”. In: *Proc. Camb. Phil. Soc. Phil. Soc.* 53 (1956), pp. 629–641.
- [138] Duncan S Callaway et al. “Network Robustness and Fragility : Percolation on Random Graphs”. In: *Phys. Rev. Lett.* 85.25 (2000), p. 5468.
- [139] Dietrich Stauffer and Amnon Aharony. *Introduction to percolation theory*. 2nd ed. 2014.
- [140] M F Sykes and J W Essam. “Exact Critical Percolation Probabilities for Site and Bond Problems in Two Dimensions”. In: *J. Math. Phys.* 5.8 (1964), p. 1117.
- [141] Scott Kirkpatrick. “Percolation and Conduction”. In: *Rev. Mod. Phys.* 45.4 (1973), p. 574.
- [142] H L Frisch, J M Hammersley, and D J A Welsh. “Monte Carlo Estimates of Percolation Probabilities for Various Lattices”. In: *Phys. Rev.* 126.3 (1962), pp. 949–951.
- [143] B Y P Dean and N F Bird. “Monte Carlo estimates of critical percolation probabilities”. In: *Proc. Camb. Phil. Soc.* 63 (1967), p. 477.
- [144] M E J Newman. “Mixing patterns in networks”. In: *Phys. Rev. E* 67 (2003), p. 026126.
- [145] Di Zhou et al. “Assortativity decreases the robustness of interdependent networks”. In: *Phys. Rev. E* 86 (2012), p. 066103.
- [146] C Schmeltzer et al. “Percolation of spatially constrained Erdos-Renyi networks with degree correlations”. In: *Phys. Rev. E* 89 (2014), p. 012116.

- [147] V Kapko, D A Drabold, and M F Thorpe. “Electronic structure of a realistic model of amorphous graphene”. In: *Phys. Status Solidi* 247.5 (2010), pp. 1197–1200.
- [148] Taishan Zhu and Elif Ertekin. “Phonons, Localization, and Thermal Conductivity of Diamond Nanothreads and Amorphous Graphene”. In: *Nano Lett.* 16 (2016), pp. 4763–4772.
- [149] Franz Bamer, Firaz Ebrahim, and Bernd Markert. “Elementary plastic events in a Zachariasen glass under shear and pressure”. In: *Materialia* 9 (2020), p. 100556.
- [150] Firaz Ebrahim, Franz Bamer, and Bernd Markert. “Vitreous 2D silica under tension : From brittle to ductile behaviour”. In: *Mater. Sci. Eng. A* 780 (2020), p. 139189.
- [151] Xiaolei Ma, Janna Lowensohn, and Justin C Burton. “Universal scaling of polygonal desiccation crack patterns”. In: *Phys. Rev. E* 99 (2019), p. 012802.
- [152] Hisao Honda. “Description of cellular patterns by Dirichlet domains: The two-dimensional case”. In: *J. Theor. Biol.* 72 (1978), pp. 523–543.
- [153] Ross Carter et al. “Pavement cells and the topology puzzle”. In: *Development* 144 (2017), pp. 4386–4397.
- [154] Sangwoo Kim et al. “Hexagonal Patterning of the Insect Compound Eye : Facet Area Variatio , Defects, and Disorder”. In: *Biophys. J.* 111 (2016), pp. 2735–2746.
- [155] C. J. Lambert and D. L. Weaire. “Theory of the arrangement of cells in a network”. In: *Metallography* 14.4 (1981), pp. 307–318.
- [156] Susmit Kumar, Stewart K. Kurtz, and Denis Weaire. “Average number of sides for the neighbours in a Poisson-Voronoi tessellation”. In: *Philos. Mag. B* 69.3 (1994), pp. 431–435.
- [157] M. Blanc and A. Mocellin. “Grain coordination in plane sections of polycrystals”. In: *Acta Metall.* 27 (1979), pp. 1231–1237.
- [158] N. Rivier. “Statistical crystallography structure of random cellular networks”. In: *Philos. Mag. B* 52.3 (1985), pp. 795–819.
- [159] Michael A. Peshkin, Katherine J. Strandburg, and Nicolas Rivier. “Entropic predictions for cellular networks”. In: *Phys. Rev. Lett.* 67.13 (1991), pp. 1803–1806.
- [160] S N Chiu. “Mean-Value Formulae for the Neighbourhood of the Typical Cell of a Random Tessellation”. In: *Adv. Appl. Probab.* 26 (1994), pp. 565–576.
- [161] J K Mason, R Ehrenborg, and E A Lazar. “A geometric formulation of the law of Aboav – Weaire in two and three dimensions”. In: *J. Phys. A* 45 (2012), p. 065001.
- [162] H. J. Hilhorst. “Planar Voronoi cells: The violation of Aboav’s law explained”. In: *J. Phys. A* 39 (2006), pp. 7227–7243.
- [163] M. E.J. Newman. “Assortative Mixing in Networks”. In: *Phys. Rev. Lett.* 89.20 (2002), pp. 1–4.
- [164] Rogier Noldus and Piet Van Mieghem. “Assortativity in complex networks”. In: *J. Complex Networks* 3 (2015), pp. 507–542.

- [165] Alexandros Chremos and Philip J. Camp. “Neighbor network in a polydisperse hard-disk fluid: Degree distribution and assortativity”. In: *Phys. Rev. E* 76 (2007), p. 056108.
- [166] Nelly Litvak and Remco van der Hofstad. “Uncovering disassortativity in large scale-free networks”. In: *Phys. Rev. E* 87 (2013), p. 022801.
- [167] J M Greneche and J M D Coey. “The topologically-disordered square lattice”. In: *J. Phys. Fr.* 51 (1990), pp. 231–242.
- [168] Franz R Eder et al. “A journey from order to disorder - atom by atom transformation from graphene to a 2D carbon glass”. In: *Sci. Rep.* 4 (2014), p. 4060.
- [169] Ordnance Survey. *Boundary-Line Data* © Crown copyright and database right 2018. 2018.
- [170] Federal Office of Topography. *swissBOUNDARIES3D*. 2019.
- [171] Eurostat. *NUTS Geodata* © EuroGeographics for the administrative boundaries. 2016.
- [172] Etienne P Bernard and Werner Krauth. “Two-Step Melting in Two Dimensions : First-Order Liquid-Hexatic Transition”. In: *Phys. Rev. Lett.* 107 (2011), p. 155704.
- [173] Andrew H Marcus and Stuart A Rice. “Phase transitions in a confined quasi-two-dimensional colloid suspension”. In: *Phys. Rev. E* 55.1 (1997), p. 637.
- [174] Han-Rui Tian et al. “An Unconventional Hydrofullerene C₆₆H₄ with Symmetric Heptagons Retrieved in Low-Pressure Combustion”. In: *J. Am. Chem. Soc.* 141 (2019), pp. 6651–6657.
- [175] Runnan Guan et al. “Stable C₉₂(26) and C₉₂(38) as Well as Unstable C₉₂(50) and C₉₂(23) Isolated-Pentagon-Rule Isomers As Revealed by Chlorination of C₉₂ Fullerene”. In: *Inorg. Chem.* 58 (2019), pp. 5393–5396.
- [176] Victor A Brotsman, Daria V Ignateva, and Sergey I Troyanov. “Chlorination-promoted Transformation of Isolated Pentagon Rule C₇₈ into Fused-pentagons- and Heptagons-containing Fullerenes”. In: *Chem Asian J* 12 (2017), pp. 2379–2382.
- [177] Victor A Brotsman et al. “Rebuilding C₆₀ : Chlorination-Promoted Transformations of the Buckminsterfullerene into Pentagon-Fused C₆₀ Derivatives”. In: *Inorg. Chem.* 57 (2018), pp. 8325–8331.
- [178] Daishi Fujita et al. “Self-assembly of tetravalent Goldberg polyhedra from 144 small components”. In: *Nature* 540 (2016), pp. 563–566.
- [179] Zhi Wang et al. “Assembly of silver Trigons into a buckyball-like Ag₁₈₀ nanocage”. In: *PNAS* 114.46 (2017), pp. 12132–12137.
- [180] A E Roth, C D Jones, and D J Durian. “Coarsening of a two-dimensional foam on a dome”. In: *Phys. Rev. E* 86 (2012), p. 021402.
- [181] P N Pusey and W Van Megen. “Phase behaviour of concentrated suspensions of nearly hard colloidal spheres”. In: *Nature* 320 (1986), p. 340.
- [182] Alice L Thorneywork et al. “Radial distribution functions in a two-dimensional binary colloidal hard sphere system”. In: *J. Chem. Phys.* 140 (2014), p. 161106.

- [183] Alice L Thorneywork et al. “Structure factors in a two-dimensional binary colloidal hard sphere system”. In: *Mol. Phys.* 116 (2018), pp. 3245–3257.
- [184] R Roth, R Evans, and A A Louis. “Theory of asymmetric nonadditive binary hard-sphere mixtures”. In: *Phys. Rev. E* 64 (2001), p. 051202.
- [185] R Y Yang, R P Zou, and A B Yu. “Voronoi tessellation of the packing of fine uniform spheres”. In: *Phys. Rev. E* 65 (2002), 041302 Voronoi.
- [186] VS Kumar and V Kumaran. “Voronoi neighbor statistics of hard-disks and hard-spheres”. In: *J Chem Phys* 123 (2005), p. 074502.
- [187] A Jaster. “Computer simulations of the two-dimensional melting transition using hard disks”. In: *Phys. Rev. E* 59.3 (1999), pp. 2594–2602.
- [188] Sander Pronk and Daan Frenkel. “Melting of polydisperse hard disks”. In: *Phys. Rev. E* 69 (2004), p. 066123.
- [189] Sebastian C Kapfer and Werner Krauth. “Two-Dimensional Melting : From Liquid-Hexatic Coexistence to Continuous Transitions”. In: *Phys. Rev. Lett.* 114 (2015), p. 035702.
- [190] Alice L Thorneywork. “Structure and dynamics of two-dimensional colloidal hard spheres”. PhD thesis. University of Oxford, 2015.
- [191] Q Weikai, A P Gantapara, and Marjolein Dijkstra. “Two-stage melting induced by dislocations and grain boundaries in monolayers of hard spheres”. In: *Soft Matter* 10.30 (2014), p. 5449.
- [192] Y Peng et al. “Short-time self-diffusion of nearly hard spheres at an oil–water interface”. In: *J Fluid Mech* 618 (2009), pp. 243–261.
- [193] N Vogel et al. “Direct visualization of the interfacial position of colloidal particles and their assemblies†”. In: *Nanoscale* 6 (2014), pp. 6879–6885.
- [194] Elisa Tamborini, C Patrick Royall, and Pietro Cicuti. “Correlation between crystalline order and vitrification in colloidal monolayers”. In: *J. Phys. Condens. Matter* 27 (2015), p. 194124.
- [195] H Imai, I Masao, and K Murota. “Voronoi Diagram in the Laguerre Geometry and its Applications”. In: *SIAM J* 14.1 (1985), pp. 93–105.
- [196] N Rivier. “Geometry and Fluctuations of Surfaces”. In: *J. Phys. Colloq.* 51 (1990), pp. 309–317.
- [197] P Bhattacharyya and B K Chakrabarti. “The mean distance to the nth neighbour in a uniform distribution of random points: an application of probability theory”. In: *Eur. J. Phys.* 29 (2008), p. 639.
- [198] L Oger et al. “Comparison of two representations of a random cut of identical sphere packing”. In: *Eur. Phys. J. B* 14 (2000), pp. 403–406.
- [199] Annie Gervois, Luc Oger, and Jean-Paul Troadec. “Random cuts in binary mixtures of spheres”. In: *Phys. Rev. E* 70 (2004), p. 031112.
- [200] U Hahn and U Lorz. “Stereological analysis of the spatial Poisson-Voronoi tessellation”. In: *J. Microsc.* 175.3 (1994), pp. 176–185.
- [201] Simone Falco et al. “Generation of 3D polycrystalline microstructures with a conditioned Laguerre-Voronoi tessellation technique”. In: *Comput. Mater. Sci.* 136 (2017), pp. 20–28.

- [202] Dorian Depriester and Régis Kubler. “Radical Voronoï tessellation from random pack of polydisperse spheres Prediction of the cells’ size distribution”. In: *Comput. Des.* 107 (2019), pp. 37–49.
- [203] Matthew O Blunt et al. “Random Tiling and Topological Defects in a Two-Dimensional Molecular Network”. In: *Science (80-.)*. 322 (2008), pp. 1077–1081.
- [204] P W Anderson. “RESONATING VALENCE BONDS" A NEW KIND OF INSULATOR?” In: *Mat. Res. Bull.* 8 (1973), pp. 153–160.
- [205] Philip J Camp, Amparo Fuertes, and J P Attfield. “Subextensive Entropies and Open Order in Perovskite Oxynitrides”. In: *J Am Chem Soc* 134 (2012), pp. 6762–6766.
- [206] R Comes, M Lambert, and A Guinier. “THE CHAIN STHUCTURE OF BaTiO3 AND KNbO3”. In: *Solid State Commun.* 6 (1968), pp. 715–719.
- [207] G Algara-Siller et al. “Square ice in graphene nanocapillaries”. In: *Nature* 519 (2015), p. 443.
- [208] YinBo Zhu, FengChao Wang, and HengAn Wu. “Structural and dynamic characteristics in monolayer square ice”. In: *J. Chem. Phys.* 147 (2017), p. 044706.
- [209] Simon J Hibble et al. “Structures of Pd (CN)2 and Pt (CN)2: Intrinsically Nanocrystalline Materials?” In: *Inorg. Chem.* 50 (2011), pp. 104–113.
- [210] Qing-Na Zheng et al. “Adaptive Reorganization of 2D Molecular Nanoporous Network Induced by Coadsorbed Guest Molecule”. In: *Langmuir* 30 (2014), pp. 3034–3040.
- [211] Lars Postulka et al. “Spin Frustration in an Organic Radical Ion Salt Based on a Kagome-Coupled Chain Structure”. In: *J. Am. Chem. Soc.* 138 (2016), pp. 10738–10741.
- [212] Ting Chen et al. “2D Hexagonal Tilings Based on Triangular and Hexagonal Structural Units in the Self-Assembly of Thiacalix[4]arene Tetrasulfonate on an Au(111) Surface”. In: *Chem Asian J* 6 (2011), pp. 1811–1816.
- [213] Austin D Griffith and Robert S Hoy. “Densest versus jammed packings of two-dimensional bent-core trimers”. In: *Phys. Rev. E* 98 (2018), p. 042910.
- [214] Jose I Urgel et al. “Five-Vertex Lanthanide Coordination on Surfaces: A Route to Sophisticated Nanoarchitectures and Tessellations”. In: *J Phys Chem C* 118 (2014), pp. 12908–12915.
- [215] N P Kryuchkov et al. “Complex crystalline structures in a two-dimensional core-softened system”. In: *Soft Matter* 14 (2018), p. 2152.
- [216] Bai-Qiao Song et al. “Periodic tiling of triangular and square nanotubes in a cationic metal – organic framework for selective anion exchange †”. In: *Chem Commun* 51 (2015), pp. 9515–9518.
- [217] William D Piñeros, Michael Baldea, and Thomas M Truskett. “Designing convex repulsive pair potentials that favor assembly of kagome and snub square lattices”. In: *J. Chem. Phys.* 145 (2016), p. 054901.

- [218] Mia Baise et al. “Negative Hydration Expansion in ZrW₂O₈ : Microscopic Mechanism, Spaghetti Dynamics, and Negative Thermal Expansion”. In: *Phys. Rev. Lett.* 120 (2018), p. 265501.
- [219] V A Gorbunov, S S Akimenko, and A V Myshlyavtsev. “Cross-impact of surface and interaction anisotropy in the self-assembly of organic adsorption monolayers : a Monte Carlo”. In: *Phys Chem Chem Phys* 19 (2017), pp. 17111–17120.
- [220] Damien Nieckarz, Wojciech Rzyso, and Paweł Szabelski. “On-surface self-assembly of tetratopic molecular building blocks”. In: *Phys Chem Chem Phys* 20 (2018), p. 23363.
- [221] C Buzano et al. “Two-dimensional lattice-fluid model with waterlike anomalies”. In: *Phys. Rev. E* 69 (2004), p. 061502.
- [222] Philip J Camp. “Structure and phase behavior of a two-dimensional system with core-softened and long-range repulsive interactions”. In: *Phys. Rev. E* 68 (2003), p. 061506.
- [223] Michael Griebel and Jan Hamaekers. “Molecular dynamics simulations of boron-nitride nanotubes embedded in amorphous Si-B-N”. In: *Comput. Mater. Sci.* 39 (2007), pp. 502–517.
- [224] Arkadiy Simonov et al. “Hidden diversity of vacancy networks in Prussian blue analogues”. In: *Nature* 578 (2020), p. 256.
- [225] Marian Florescu, Salvatore Torquato, and Paul J Steinhardt. “Designer disordered materials with large, complete photonic band gaps”. In: *PNAS* 106.49 (2009), pp. 20658–20663.
- [226] Steven R Sellers et al. “Local self-uniformity in photonic networks”. In: *Nat. Commun.* 8 (2017), p. 14439.
- [227] Herbert Edelsbrunner and John Harer. “Persistent homology - a survey”. In: *Contemp. Math.* 453 (2008), p. 257.
- [228] Benjamin M G D Carter et al. “Structural covariance in the hard sphere fluid”. In: *J. Chem. Phys.* 148 (2018), p. 204511.
- [229] V Robins et al. “Pore configuration landscape of granular crystallization”. In: *Nat. Commun.* 8.May (2017), pp. 1–11.
- [230] Fei Jiang, Takeshi Tsuji, and Tomoyuki Shirai. “Pore Geometry Characterization by Persistent Homology Theory”. In: *Water Resour. Res.* 54 (2018), pp. 4150–4163.
- [231] Lee Steinberg, John Russo, and Jeremy Frey. “A new topological descriptor for water network structure”. In: *J. Cheminform.* 11.48 (2019), pp. 1–11.
- [232] Kelin Xia et al. “Persistent Homology for the Quantitative Prediction of Fullerene Stability”. In: *J. Comput. Chem.* 36 (2015), pp. 408–422.
- [233] Yasuaki Hiraoka et al. “Hierarchical structures of amorphous solids characterized by persistent homology”. In: *PNAS* 113.26 (2016), pp. 7035–7040.
- [234] Yohei Onodera et al. “Understanding diffraction patterns of glassy, liquid and amorphous materials via persistent homology analyses”. In: *J. Ceram. Soc. Japan* 127.12 (2019), pp. 853–863.

- [235] Takenobu Nakamura et al. “Persistent homology and many-body atomic structure for medium-range order in the glass”. In: *Nanotechnology* 26 (2015), p. 304001.
- [236] Abraham Gutierrez, Mickaël Buchet, and Sylvain Clair. “Persistent Homology To Quantify the Quality of Surface- Supported Covalent Networks”. In: *ChemPhysChem* 20 (2019), pp. 1–7.
- [237] The GUDHI Project. *GUDHI User and Reference Manual*. 3.2.0. GUDHI Editorial Board, 2020.
- [238] Ulderico Fugacci et al. “Persistent homology: a step-by-step introduction for newcomers”. In: *Smart Tools Apps Comput. Graph.* October (2016).
- [239] Nina Otter et al. “A roadmap for the computation of persistent homology”. In: *EPJ Data Sci.* 6 (2017), p. 1.
- [240] Afra Zomorodian and Gunnar Carlsson. “Computing Persistent Homology”. In: *Discret. Comput Geom* 33 (2005), pp. 249–274.
- [241] Joseph O’Rourke. *Computational geometry in C*. 2nd ed. Cambridge core. Cambridge, UK ; New York, NY, USA: Cambridge University Press, 1998.